7-16-1992

Enhancements to atmospheric-correction techniques for multiple thermal images

Robert J. Mericsko

Follow this and additional works at: http://scholarworks.rit.edu/theses

ENHANCEMENTS TO ATMOSPHERIC-CORRECTION TECHNIQUES FOR MULTIPLE THERMAL IMAGES

by

Robert J. Mericsko

B.S. – Rochester Institute of Technology

(1970)

M.S. – The George Washington University

(1975)

Submitted to the
Center for Imaging Science
in partial fulfillment of the requirements
for the Master of Science degree
at the Rochester Institute of Technology

July 16, 1992

Signature of the Author____Robert J. Mericsko_____

Accepted by_____

Coordinator, M.S. Degree Program

College of Imaging Arts and Sciences
Rochester Institute of Technology
Rochester, New York

Certificate of Approval

M.S. DEGREE THESIS

The M.S. degree thesis of Robert J. Mericsko
has been examined and approved by the
thesis committee as satisfactory for the
thesis requirement of the
Master of Science degree

Dr. John R. Schott, Thesis Advisor

Dr. Mark Fairchild

Mr. Carl Salvaggio

7/16/92

Date

Thesis Release Permission

Rochester Institute of Technology

College of Imaging Arts and Sciences

Title of Thesis: *Enhancements to Atmospheric-correction Techniques for Multiple Thermal Images.*

I, Robert J. Mericsko, hereby grant permission to the Wallace Memorial Library of R.I.T. to reproduce my thesis in whole or in part. Any reproduction will not be for commercial use or profit.

Date: *July 16, 1992*

Abstract

Statistical estimation problems of atmospheric correction techniques for thermal infrared imagery have been studied. A revised multiple-view-angle atmospheric correction technique has been developed and tested using the LOWTRAN radiative transfer model as truth. Its average absolute temperature prediction accuracy for an independent data set is 0.8 K for long-wave infrared imagery and 1.0 K for mid-wave infrared imagery, when error-free data are assumed. The benefit of robust, resistant regression estimators was studied using Monte Carlo simulations having real-world measurement errors and data outliers. An error propagation analysis showed that 1.0–3.3 K of rms error is likely given reasonable data set sizes and robust estimators.

Acknowledgements

Dedication

I dedicate this thesis to the three women in my life, my daughters Anne and Elizabeth, and especially my wife Janie. Their patience throughout my three–year sabbatical at R.I.T. was much appreciated. I owe them many years of "quality time" in return.

Table of Contents

List of Symbols

A_λ . . . Spectral attenuation [unitless]

D . . . (Optical) density [d]

e . . . Error component

G . . . Sensor's gain factor [degrees K volt^{-1}]

H . . . Nadir distance [ft]

i . . . . Index [unitless]

J . . . Total number of altitudes [unitless]

j . . . . Altitude index [unitless]

K . . . Total number of view angles [unitless]

k . . . View angle index [unitless]

L . . . Radiance [W m^{-2} sr^{-1}]

$\hat{L}$ Estimated radiance [W·m^{-2}·sr^{-1}]

L_D . . . (Effective) downwelled radiance [W m^{-2} sr^{-1}]

$\hat{L}_D$ . . . Estimated (effective) downwelled radiance [W m^{-2} sr^{-1}]

$L_{D\lambda}$ . . . Downwelled spectral radiance [W m^{-2} sr^{-1} μm^{-1}]

L_T . . . (Effective) blackbody-equivalent radiance [W m^{-2} sr^{-1}]

$\hat{L}_T$ Estimated (effective) blackbody-equivalent radiance [W·m^{-2}·sr^{-1}]

$L_{T\lambda}$ . . . Blackbody-equivalent spectral radiance [W m^{-2} sr^{-1} μm^{-1}]

L_U . . . (Effective) upwelled radiance [W m^{-2} sr^{-1}]

$\hat{L}_U$ . . . Estimated upwelled radiance [W m^{-2} sr^{-1}]

$L_{U\lambda}$ . . . Upwelled spectral radiance [W m^{-2} sr^{-1} μm^{-1}]

N . . . Total number of input variables [unitless]

n . . . Input variable index [unitless]

R_i . . . Spectrally weighted mean sensitivity of sensor [unitless]

R_λ . . . Relative spectral sensitivity of sensor [unitless]

S_λ . . . Spectral radiance of the source [W m^{-2} sr^{-1} μm^{-1}]

T . . . Apparent Temperature [degrees K]

T_{bb} . . . Blackbody temperature [degrees K]

V . . . Imaging scanner's voltage [v]

V_{bb} . . . Scanner's voltage for a blackbody [v]

V_0 . . . Intercept term of density-voltage calibration [v]

X . . . Independent variable

Y . . . Dependent variable

$\hat{\beta}_0$ . . . Least-squares estimator of unknown intercept term β_0

$\hat{\beta}_1$ . . . Least-squares estimator of unknown slope term β_1

$\bar{\beta}_0$ . . . Max-likelihood estimator of unknown intercept term β_0

$\bar{\beta}_1$ . . . Maximum-likelihood estimator of unknown slope term β_1

$\ddot{\beta}_0$ . . . Biweight estimator of unknown intercept term β_0

$\ddot{\beta}_1$ . . . Biweight estimator of unknown slope term β_1

γ_i . . . Slope term of ith segment of density-voltage calibration

ε . . . . (Effective) emissivity [unitless]

ε_λ . . . Spectral emissivity [unitless]

ζ . . . Object tilt angle from nadir [degrees]

θ . . . View angle from nadir [degrees]

λ . . . Wavelength [μm]

λ_1 . . . Lower bound on spectral sensitivity of sensor [μm]

λ_2 . . . Upper bound on spectral sensitivity of sensor [μm]

ρ_λ . . . Spectral reflectivity of an object [unitless]

$\hat{\sigma}$ . . . Estimator of the standard error

τ . . . . (Effective) atmospheric transmittance [unitless]

$\hat{\tau}$ . . . . Estimator of atmospheric transmittance [unitless]

τ_λ . . . Atmospheric spectral transmittance [unitless]

ϕ . . . Azimuth angle [degrees]

List of Figures

List of Tables

1. INTRODUCTION AND SUMMARY

1.1 Introduction

Thermal infrared imagery from aircraft and satellites has been used extensively in hydrologic, land use, and heat loss studies. In many of these remote sensing applications, the quantitative assessment of surface (and internal) temperatures is desired. In these cases, atmospheric correction techniques must be employed.

1.2 Summary

The statistical estimation problems of atmospheric correction techniques have been studied, and an enhanced multiple-view-angle atmospheric correction technique has been developed and tested. Its average absolute temperature prediction error for an independent data set is 0.8 K for long-wave infrared (LWIR) and 1.0 K for mid-wave infrared (MWIR) imagery acquired at night. The effect of data outliers on the estimates of atmospheric transmittance and upwelled radiance are significant, especially for sample sizes smaller than 20. A positive bias of 0.24–0.80 K, relative to an object at 295 K, was found. The use of a robust and resistant regression algorithm, Tukey's biweight, reduced the effect; the positive bias was reduced to 0.13–0.53 K. An end-to-end error propagation computer program was developed. Given real-world error component values, the regression coefficients, and consequently the atmospheric transmittance and upwelled radiance estimators, were the most significant components, accounting for greater than 86% of the total rms error.

2. BACKGROUND

2.1 Historical Background

The influence of the atmosphere in attenuating signals has been recognized since 1942 when Elassen studied carbon dioxide and water absorption band theory [Chedin et al. (1982)]. Further work, in that time period, was done by Chapman et al. (1949), but little more was published until the late 1960s [Haynes and Whipple (1971)].

One of the first to publish an empirical technique for determining atmospheric correction was Saunders (1967). He used a non-scanning radiometer, flown at a 300 m altitude, to observe a thermally stable sea surface. He found that, at a 60° view angle, the attenuation was twice the value at nadir. Saunders (1970) established that the influence of haze was insignificant when using this technique. Simple extensions of his technique were suggested by Tien (1974). Chedin et al. (1982) used a dual-view-angle technique for the determination of sea surface temperature from two satellites, one in geostationary orbit and the other in polar orbit.

Lorenz (1968), in an article describing the use of radiometers to measure the temperature of natural surfaces, stated that the most significant sources of error were the target reflectivity, as a function of view angle, and the intervening air layer. From an analysis of low altitude aircraft flight experiments, he produced a set of atmospheric correction curves based on the difference between the surface and air temperatures at constant relative humidity and altitude. Recently, Cogan (1985 and 1988) has also developed an atmospheric correction technique based on

the air temperature at flight altitude.

Scarpace and Green (1973), and Scarpace et al. (1975), in studies of thermal plumes in water, were among the first to use extensive ground-truth measurements in an atmospheric correction technique. They used the maximum and minimum temperatures recorded by a boat-mounted portable radiometric thermometer to calibrate a thermal imaging scanner flown in an aircraft. For their 1975 calibration work, they used both water temperature measurements from three-meter diameter pools of thermally stable water located at a target site and lake measurements routinely gathered by the power company.

Prabhakara et al. (1974) devised an atmospheric correction technique for sea-surface temperature estimation based on a model of the differential absorption properties of water vapor. Using data from 106 different geographic locations acquired by a Nimbus infrared interferometer spectrometer, they simulated measurements to optimize the selection of two wavelength bands. McMillan (1975) used a similar approach, but he added the partial pressure of water to his own water-absorption model. Techniques using multiple spectral bands have continued to be a subject of study [Price (1984), Singh (1984), Dalu (1986), and Wan and Dozier (1989)].

Schott and Tourin (1975) devised an atmospheric calibration method which relied on establishing an atmospheric absorption profile, which was then extrapolated to zero altitude. This "profile method" has been employed in numerous studies, with reported accuracies of better than 0.5 K [e.g., Schott (1979)]. Macleod (1984), building on this work, demonstrated the applicability of a dual-view-angle technique for objects

other than just sea water [Cf. Chedin et al. (1982)]. Byrnes (1983) and Byrnes and Schott (1986) compared the profile and dual-view-angle techniques to the then current version of the radiative-transfer model LOWTRAN [Kneizys et al. (1980)]. Within the past decade, multiple-view techniques (either with respect to altitude or angle) have been developed by Maul (1981), Price (1983), Holyer (1984), Diner and Martonchik (1985), Steven and Rollin (1986), Wilson and Anderson (1986), and Djavadi and Anderson (1987). These last two papers are interesting in that they document an aerial thermographic survey, used to determine building heat loss, where the variation in surface temperature with time was the dominant source of error.

The following paragraphs concentrate on the multiple-view-angle techniques. Given an airborne imaging sensor, multiple-view-angle acquisitions are generally cheaper than multiple-altitude ones. Given a satellite imaging sensor, multiple-view-angle acquisitions are generally the only option. Many airborne and satellite sensor systems are designed to provide either side-to-side or front-to-back views of the same geographic area. A special effort will be made throughout this thesis to characterize the effects of the error components on the statistical parameter estimation process.

2.2 Calculation of Direct Effective Radiance

The direct effective radiance $L(H,\theta)$ onto a thermal infrared imaging sensor at nadir distance H and view angle from nadir θ is given by the equation,

$$L(H,\theta) = \int_{-\infty}^{\infty} S_\lambda A_\lambda(H,\theta) R_\lambda \, d\lambda, \tag{1}$$

where S_λ is the spectral radiance of the source, $A_\lambda(H,\theta)$ is the spectral attenuation, and R_λ is the relative spectral sensitivity of the sensor. One of the complexities of earth remote sensing in the thermal infrared is that multiple sources are involved. This is usually not the case in either visible or microwave remote sensing. A model that considers an object, the downwelling of the sky and object background, and the upwelling of the atmospheric path as three additive thermal sources has been studied by Schott (1979), Byrnes (1983), and Macleod (1984). It can be written as

$$L(H,\theta) = \int_{\lambda_1}^{\lambda_2} \left\{ \left[L_{T\lambda}\, \varepsilon_\lambda(\theta,\zeta,\phi) + L_{D\lambda}\, \rho_\lambda(\theta,\zeta,\phi) \right] \tau_\lambda(H,\theta) + L_{U\lambda}(H,\theta) \right\} R_\lambda\, d\lambda, \quad (2)$$

where $L_{T\lambda}\, \varepsilon_\lambda$ is the graybody-equivalent spectral radiance of an object, $L_{D\lambda}$ is the downwelled spectral radiance, $L_{U\lambda}$ is the upwelled spectral radiance, $\rho_\lambda \cdot \tau_\lambda$ is the spectral attenuation of the downwelled radiance, $L_{T\lambda}$ is the blackbody-equivalent spectral radiance, ε_λ is the spectral emissivity of an object, ρ_λ is its spectral reflectivity, ζ is its tilt angle from nadir, ϕ is its azimuth angle, τ_λ is the atmospheric spectral transmittance, and λ_1 and λ_2 define the spectral bandpass of the sensor. Equation (2) can be approximated by

$$L(H,\theta) = \tau(H,\theta)\, L(0,\theta) + L_U(H,\theta), \quad (3)$$

where

$$L(0,\theta) = \int_{\lambda_1}^{\lambda_2} \left[L_{T\lambda}\, \varepsilon_\lambda(\theta,\zeta,\phi) + L_{D\lambda}\, \rho_\lambda(\theta,\zeta,\phi) \right] R_\lambda\, d\lambda, \quad (4)$$

$$L_U(H,\theta) = \int_{\lambda_1}^{\lambda_2} L_{U\lambda}(H,\theta)\, R_\lambda\, d\lambda, \quad (5)$$

and, using the mean-value theorem for an integral,

$$\tau(H,\theta) = \frac{1}{\lambda_2 - \lambda_1} \int_{\lambda_1}^{\lambda_2} \tau_\lambda(H,\theta)\, d\lambda. \quad (6)$$

5

Note that the mean-value theorem for an integral is valid only for continuous functions. Consequently, the applicability of Equation (3) holds strictly only for spectral regions of the atmosphere where neither absortion nor emission lines exist.

The following subsections will essentially follow Schott (1989) in the development of three special cases of Equation (3), but with more emphasis on the statistical assumptions and error components in the models.

2.2.1 Given Ground-truth Data

If high-precision ground-truth measurements of I objects at different graybody-equivalent radiances are available (i.e., $\{L_i(0,\theta)\}$, $i=1,2,...,I$) and if the measurement error e_i on each dependent variable's observation $L_i(H,\theta)$ is additive, then Equation (3) can be written as a first-order linear equation

$$L_i(H,\theta) = \tau(H,\theta)\, L_i(0,\theta) + L_U(H,\theta) + e_i. \tag{7}$$

Assuming the atmospheric effects are spatially and temporally consistent over the imagery set and that both H and θ are fixed constants, then the minimum-variance linear unbiased estimates of τ and L_U can be determined by a least-squares regression of $\{L_i(H,\theta)\}$ onto $\{L_i(0,\theta)\}$. Figure 1 shows the effect of altitude, temperature and view angle on direct effective radiance (excluding the downwelled radiance component) for a long-wave infrared sensor and a midlatitude-summer atmosphere.

Figure 1: Effect of temperature and view angle on radiance at 1000'
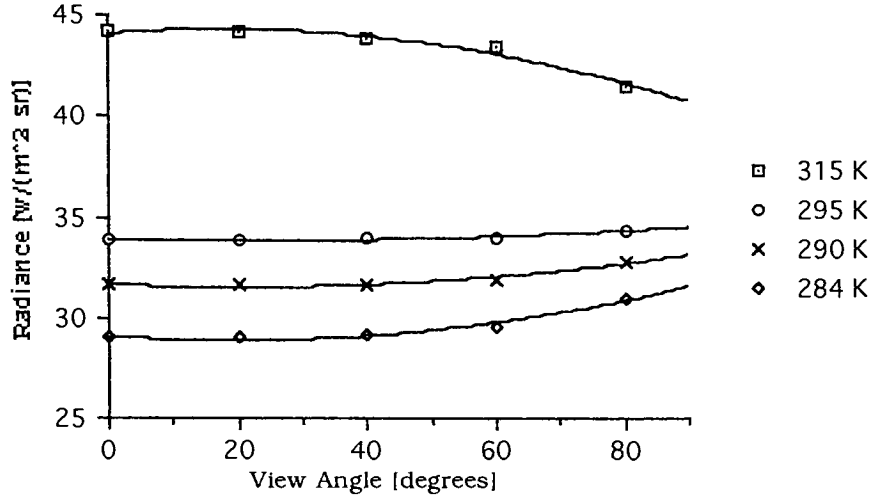
Figure 2 demonstrates the reasonability of the least-squares regression solution using Equation 7 and data from four objects. Since the data comes from computer runs of the LOWTRAN 7 model [Kneizys et al. (1988)], there is no measurement error. Therefore, the regression is perfect, i.e., the estimator $\hat{\tau} = \tau$ and the estimator $\widehat{L_U} = L_U$.

Figure 2: Least-squares fit to 1000' data

7
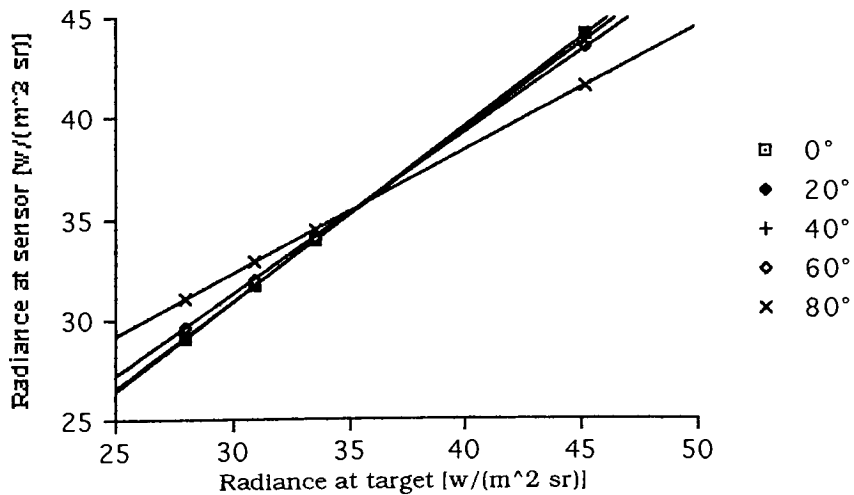
2.2.2 Given Multiple-altitude Data

In the absence of ground truth, but with I objects at different graybody-equivalent radiances imaged at J different altitudes (i.e., $\{L_i(H_j,\theta)\}$, $i=1,2,\ldots,I$, $j=1,2,\ldots,J$) and all at the same view angle θ, Equation (3) can be written as

$$L_i\left(H_j,\theta\right) = \tau\left(H_j,\theta\right) L_i\left(0,\theta\right) + L_U\left(H_j,\theta\right) + e_{ij}, \qquad (8)$$

where $L_i\left(0,\theta\right)$ is a high-precision calculated radiance of object i at ground level and view angle θ, e_{ij} is the additive error on the dependent variable's observation, $L_i\left(H_j,\theta\right)$. One constraint, that is often useful as a calculation check, is

$$0 \le \tau\left(H_{j+1},\theta\right) \le \tau\left(H_j,\theta\right) \le 1 = \tau\left(0,\theta\right) \qquad (9)$$

where $H_j < H_{j+1}$.

The profile technique (Schott and Tourin 1975) considers the case for Equation 8 where $\theta = 0$, and assumes $L_i(0,0)$ can be estimated with high precision as the intercept of a previous regression of $\{L_i(H_j,0)\}$ onto $\{H_j\}$. The function used in the first regression is established by comparison of the observed radiances to a series of curves predicted using the LOWTRAN atmospheric model for a range of apparent temperatures. Figure 3 shows an example of this first step. Although not necessary, the availability of radiosonde and ground-truth data substantially aids in selecting the best LOWTRAN cases to be run. Analogous to the solution for Equation 7, estimates of $\tau(H_j,0)$ and $L_U(H_j,0)$ in Equation 8 are then calculated by a least-squares regression of $\{L_i(H_j,0)\}$ onto the estimates of $\{L_i(0,0)\}$.

8

Figure 3: Profile technique used to estimate L(0,0)
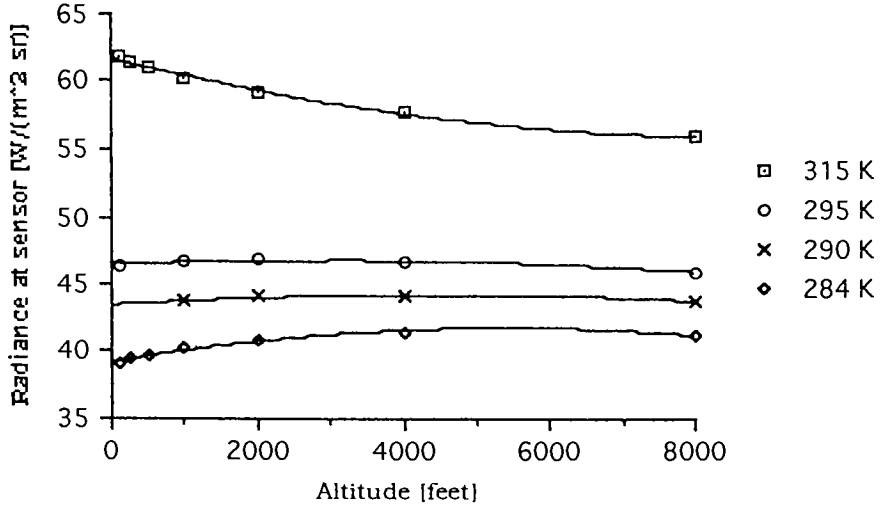
2.2.3 Given Multiple-view-angle Data

Again in the absence of ground truth, consider the case of I objects at different graybody-equivalent radiances, but imaged at K different view angles (i.e., $\{L_i(H,\theta_k)\}$, $i = 1,2,...,I$, $k = 1,2,...,K$) and all at the same altitude H. Assuming that these objects are Lambertian (i.e., $L_i(0,\theta_k) = L_i(0,0)$), Equation 3 can be written as

$$L_i(H,\theta_k) = \tau(H,\theta_k) L_i(0,0) + L_U(H,\theta_k) + e_{ik} \qquad (10)$$

where $L_i(0,0)$ is the radiance of the ith object at ground level and e_{ik} is the additive measurement error in the dependent variable's observation $L_i(H,\theta_k)$. Assuming that at one constant view angle, say θ_1, $L_i(H,\theta_k)$ is known with high precision (i.e., $e_{i1} \cong 0$), then Equation 10 can be written as

$$L_i(H,\theta_1) = \tau(H,\theta_1) L_i(0,0) + L_U(H,\theta_1). \qquad (11)$$

Using Equation 11 to solve for $L_i(0,0)$ and substituting back into Equation 10 gives another first-order linear equation

$$L_i(H,\theta_k) = \beta_1 \, L_i(H,\theta_1) + \beta_0 + e_{ik}, \tag{12}$$

where

$$\beta_1 = \frac{\tau(H,\theta_k)}{\tau(H,\theta_1)} \tag{13}$$

and

$$\beta_0 = L_U(H,\theta_k) - \frac{\tau(H,\theta_k)}{\tau(H,\theta_1)} L_U(H,\theta_1). \tag{14}$$

Assuming that the atmospheric effects are spatially and temporally consistent, the minimum-variance linear unbiased estimates of β_1 and β_0 in Equation 12 can be found by a least-squares regression of $\{L_i(H,\theta_k)\}$ onto $\{L_i(H,\theta_1)\}$.

Consider the case where $\theta_1 = 0$ and the Bouguer-Lambert Law models well the effective atmospheric transmittance, i.e.,

$$\tau(H,\theta_k) = \tau(H,0)^{\sec\theta_k}. \tag{15}$$

Substituting Equation 15 into Equation 13 gives as an estimator of $\tau(H,0)$

$$\widehat{\tau}(H,0) = \widehat{\beta_1}^{\,1/(\sec\theta_k - 1)}. \tag{16}$$

In addition, if the upwelled radiance is simplistically considered as coming from a finite number of sources where, as the path length increases, the effective number of sources increases by the reciprocal of the view angle, then

$$L_U(H,\theta_k) = L_U(H,0) \sec\theta_k. \tag{17}$$

Substituting Equations 17 and 13 into Equation 14 gives as an estimator of $L_U(H,\theta)$

$$\widehat{L_U}(H,0) = \frac{\widehat{\beta_0}}{\sec\theta_k - \widehat{\beta_1}}. \tag{18}$$

Schott et al. (1983) have proposed a modification to Equation 17, for modeling $L_U(H,\theta)$, based on a layered-atmosphere model. Their

modified equation is

$$L_U(H,\theta_k) = L_U(H,0)\, \sec\theta_k \; \tau(H,0)^{\sec\theta_k - 1}. \tag{19}$$

Using the same approach as in the previous paragraph, gives

$$\widehat{L}_U(H,0) = \frac{\widehat{\beta_0}}{\widehat{\beta_1}\left[\sec\theta_k - 1\right]}. \tag{20}$$

2.3 Calculation of Apparent Temperature

Using Equations 3, 16, and either 18 or 20, $L(0,0)$ can be estimated by

$$\widehat{L}(0,0) = \frac{L(H,0) - \widehat{L}_U(H,0)}{\widehat{\tau}(H,0)}. \tag{21}$$

For a non-transparent, Lambertian object, $\varepsilon_\lambda(\theta,\zeta,\phi) = 1 - \rho_\lambda(\theta,\zeta,\phi) = \varepsilon_\lambda$. Using Equation 4, and estimates of ε and L_D, L_T can be estimated by

$$\widehat{L}_T = \frac{L(0,0) - \widehat{L}_D\left(1 - \widehat{\varepsilon}\right)}{\widehat{\varepsilon}}, \tag{22}$$

where

$$L_T = \int_{\lambda_1}^{\lambda_2} L_{T\lambda}\, R_\lambda\, d\lambda, \tag{23}$$

$$L_D = \int_{\lambda_1}^{\lambda_2} L_{D\lambda}\, R_\lambda\, d\lambda, \tag{24}$$

and, using the mean-value theorem for an integral,

$$\varepsilon = \frac{1}{\lambda_2 - \lambda_1} \int_{\lambda_1}^{\lambda_2} \varepsilon_\lambda\, d\lambda. \tag{25}$$

The mean-value theorem for an integral applies only if ε_λ is a continuous function; it is a reasonable assumption for real-world objects.

Since the sensor operates as an integrator of Planck's Law over its spectral sensitivity range, i.e.,

$$L_T = \int_{\lambda_1}^{\lambda_2} \frac{c_1}{\lambda^5 \left[\exp\left(\frac{c_2}{\lambda T}\right) - 1 \right]} R_\lambda \, d\lambda, \tag{26}$$

where $c_1 = 1.1911 \times 10^{-16}$ W m^2 sr^{-1} and $c_2 = 1.4388 \times 10^{-2}$ m K, a look-up table can be made to estimate T from L_T.

Summarizing what has been accomplished in Section 2, after giving a literature review of atmospheric-correction techniques for thermal imagery, the step-by-step equations were developed to derive the apparent blackbody temperatures of objects from their measured direct effective radiances at the sensor. Three cases were detailed: 1) given ground truth, i.e., radiance measurements of the objects at zero altitude; 2) given multiple images at various altitudes and constant view angle; and 3) given multiple images at various view angles and constant altitude. The next section describes potential enhancements, with particular emphasis on multiple-view-angle imagery.

3. APPROACH

A review of the literature on this topic suggested a number of potential enhancements. They can be grouped as enhancements to either the multiple-view-angle technique (Equation 15 and either Equation 17 or 19) or for statistical estimation (Equation 12). Proposed enhancements will be discussed in Sections 3.2 and 3.3. Prior to that, however, Section 3.1 will discuss the generation of the database upon which the enhancements were made. Finally, Section 3.4 discusses the derivation of the error propagation equations through the entire multiple-view-angle atmospheric correction procedure.

3.1 Simulations and LOWTRAN 7

Generation of the data for developing and testing improvements to the multiple-view-angle technique was via the Center for Imaging Science's user-friendly version of LOWTRAN 7 [Kneizys et al. (1988)], termed DIRTRAN. LOWTRAN is an atmospheric radiation propagation model, written in FORTRAN, that has been undergoing field measurement validation and refinement for over twenty years at the Air Force Geophysics Lab. It is a <u>low</u> spectral resolution band model originally used only to calculate <u>tran</u>smission (hence the name LOWTRAN) for a specified path through the atmosphere. Since version 4, LOWTRAN also calculates radiance. LOWTRAN 7 covers the spectral range from 0.2 μm to 20 μm. It includes all the important physical mechanisms (except for turbulence): molecular, aerosol, fog, rain, and cloud absorption and scattering.

The data for developing the enhancements (the dependent data set) came from simulations run for a variety of atmospheric, acquisition geometry, blackbody temperature, and sensor spectral response conditions. Three LOWTRAN standard atmospheres, tropical, midlatitude summer and subartic winter, were chosen to span the range of geographic and seasonal conditions. A total of 480 computer runs were made. They include all combinations of four altitudes (1000 ft, 2000 ft, 4000 ft and 8000 ft) by five view angles (0°, 20°, 40°, 60° and 80°) by four temperatures. For the tropical and midlatitude summer atmospheres, the blackbody temperatures were 284 K, 290 K, 295 K and 315 K. For the subartic winter atmosphere, the blackbody temperatures were 250 K, 265 K, 270 K and 280 K. Two spectral sensitivity distributions were used, one for a long-wave infrared (LWIR) sensor and the other for a mid-wave infrared (MWIR) sensor. They are shown in Figures 4 and 5.

Figure 4: LWIR sensor's spectral response
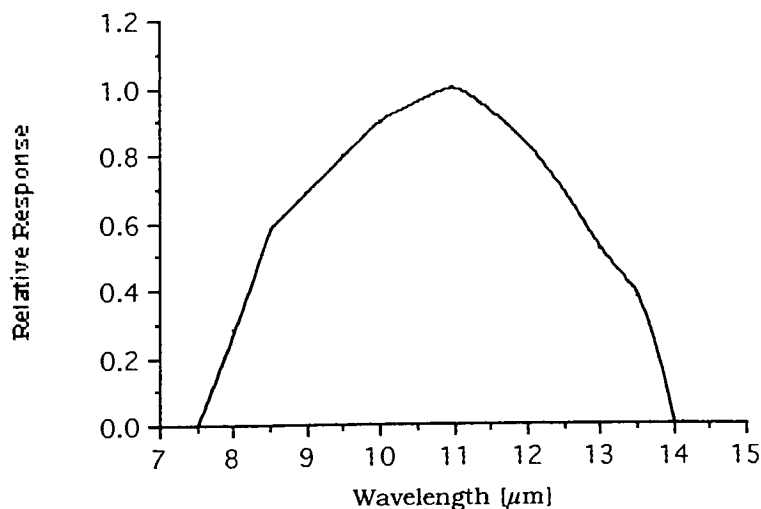
Figure 5: MWIR sensor's spectral response
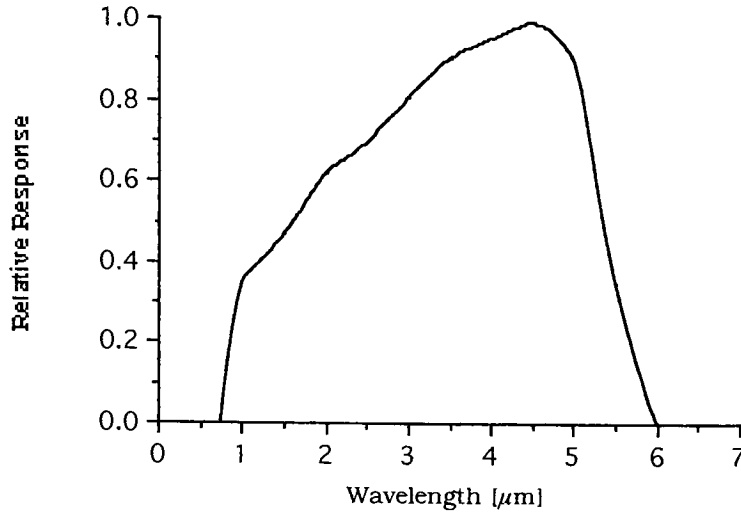
The LWIR sensor is a mercury-cadmium-telluride (HgCdTe) detector (serial number G-2370), used on the RIT aircraft. The MWIR sensor is an indium-antimonide (InSb) photovoltaic detector, representative of one planned for future flights. The object emissivity was fixed at 0.90 for the LWIR cases and 0.85 for the MWIR cases.

The standard DIRTRAN run produces 14 pages of output. The code was modified to eliminate most of the print statements. Tables A1 and A2 in Appendix A summarize the dependent data set.

The data for validating the enhancements (the independent data set) were from a similar set of LOWTRAN 7 runs (same altitudes, view angles and temperatures), but varying either the atmospheric condition, the object emissivity, or both the atmosphere and emissivity. Five cases were run for both a LWIR and MWIR sensor, giving a total of 800 validation runs. Case 1 uses the LOWTRAN standard midlatitude summer atmosphere with an object emissivity of 0.986, typical of water.

Cases 2–5 use radiosonde measurements instead of the LOWTRAN standard atmospheres: 20 June 1984 data for Case 2; 22 June 1984 data for Case 3; 6 October 1984 data for Case 4; and 24 February 1987 data for Case 5. For the LWIR runs, cases 2–5 use $\varepsilon = 0.90$. For the MWIR runs, cases 2 and 3 use $\varepsilon = 0.85$, and cases 4 and 5 use $\varepsilon = 0.90$. Tables A3 and A4 in Appendix A summarize the independent data set.

3.2 Multiple-view-angle Technique

Both Equations 15 and 17 are simplistic models of reality, especially for dense atmospheres and for view angles beyond 60°. This is demonstrated in Figures 6 and 7. Figure 6 shows the predicted and actual atmospheric transmittance as a function of view angle; Figure 7 shows a similar plot for upwelled radiance. Using the data from Tables A1 and A2, a number of alternative models were investigated; they are summarized in Tables 1 and 2.

Figure 6: Simple secant correction for atmospheric transmittance (LWIR data, midlatitude summer, 8000 ft)

16
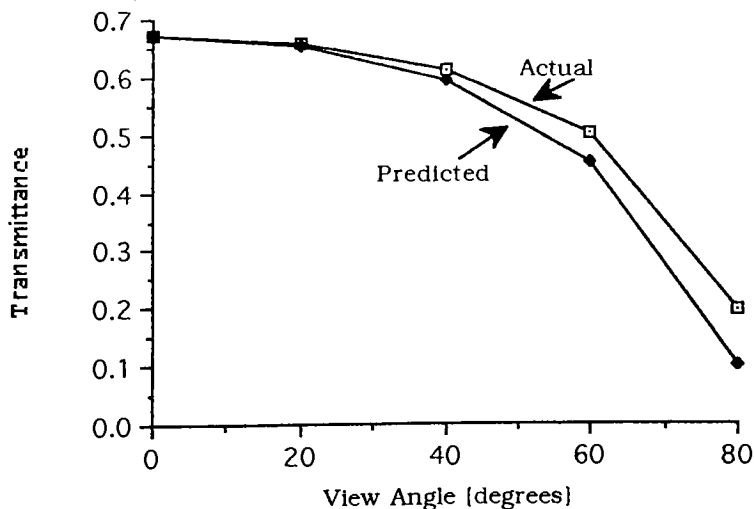
Figure 7: Simple secant correction for upwelled radiance (LWIR data, midlatitude summer, 8000 ft)
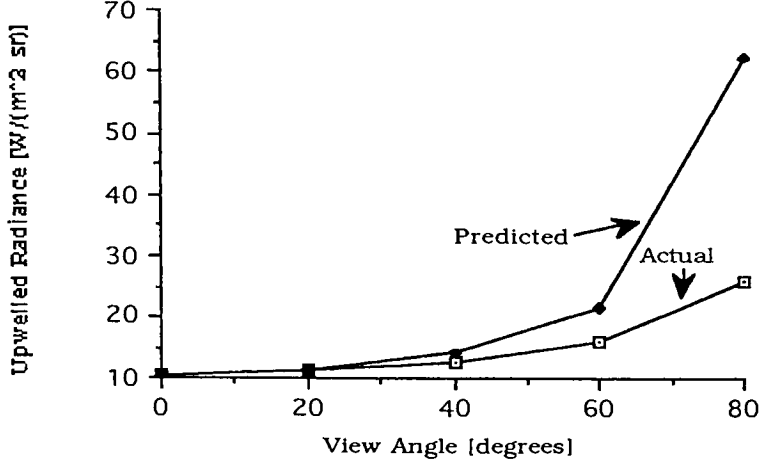
Table 1: Alternative models for atmospheric transmittance

Model 1–Simple secant:

$$\tau(H,\theta) = \tau(H,0)^{\sec\,\theta} \tag{27}$$

Model 2–Optical depth:

$$\tau(H,\theta) = \kappa_0 + \kappa_1 \log\!\left[-\log\!\left\{\tau(H,0)^{\sec\,\theta}\right\}\right] \tag{28}$$

Model 3–Altitude and secant:

$$\tau(H,\theta) = \log\left[H^{\kappa_1}\left(\sec\,\theta\right)^{\kappa_2}\right] \tag{29}$$

Model 4–Linear correction of secant:

$$\tau(H,\theta) = \tau(H,0)^{\kappa_0\,+\,\kappa_1\,\sec\,\theta} \tag{30}$$

Model 5–Multiplicative correction of secant:

$$\tau(H,\theta) = \tau(H,0)^{\kappa_1}\left[\sec\,\theta\right]^{\kappa_2} \tag{31}$$

Model 6–Secant-to-a-power correction:

$$\tau(H,\theta) = \tau(H,0)^{\left[\sec\,\theta\right]^{\kappa}} \tag{32}$$

17

Model 1–Simple secant:

$$L_U(H,\theta) = L_U(H,0) \sec \theta \tag{33}$$

Model 2–Schott's model:

$$L_U(H,\theta) = L_U(H,0) \sec \theta \, \tau(H,0)^{\sec \theta - 1} \tag{34}$$

Model 3–Byrnes' model:

$$L_U(H,\theta) = L_U(H,0) \, \frac{3 + 2 \, \tau(H,0)^{\sec \theta - 1} - \tau(H,0)}{4 \cos \theta} \tag{35}$$

Model 4–Secant-to-a-power correction:

$$L_U(H,\theta) = L_U(H,0) \left[\sec \theta\right]^\kappa \tag{36}$$

Model 5–Linear function of atmospheric transmittance:

$$L_U(H,\theta) = \kappa \left[1 - \tau(H,\theta)\right] \tag{37}$$

Model 6–Linear function of Schott's model:

$$L_U(H,\theta) = \kappa_0 + \kappa_1 \left[L_U(H,0) \sec \theta \, \tau(H,0)^{\sec \theta - 1}\right] \tag{38}$$

Model 7–Modified Schott's model:

$$L_U(H,\theta) = L_U(H,0) \left[\sec \theta \, \frac{\tau(H,\theta)}{\tau(H,0)}\right]^\kappa \tag{39}$$

The optical depth model of atmospheric transmittance, Equation 28, is based on the LOWTRAN 5 development work of Kneizys et al. (1980). Specifically, in their Section 5.1, they showed that, except for the very high or very low values, transmittance is a first-order linear function of the logarithm of the equivalent optical depth. Model 3, Equation 29, is a simplification of the optical depth model and is an attempt to lessen the adverse effect of taking a logarithm of a logarithm. Models 4–6 (Equations 30–32) are various attempts to reduce the effect of the secant power term in Model 1.

Byrnes (1983) developed Equation 35 (Model 3) for $L_U(H,\theta)$ based on a multi-layered atmosphere that appeared to model high view angles

better than Equations 33 and 34. He, however, did not test out his equation. Similar to the above attempts to reduce the effect of the secant term, Models 4–7 (Equations 36–39) were developed and analyzed.

Many of the alternative models require empirical coefficients. They were derived via regression analyses using the well-known statistical package, SAS [SAS Institute (1985)], which was run on a DEC VAX 8650 computer at RIT. All data analysis software was originally written in Fortran and run on the DEC VAX system at RIT. It was subsequently rewritten to Think C™, an ANSI-conformant version of C for the Apple Macintosh® computer.

3.3 Statistical Estimation

Good parameter estimators have the qualities of being unbiased, robust and resistant. Bias relates to the deviation of the expected value of the estimator from the true value. Robustness relates to the sensitivity of the estimator to the assumed distribution of errors, e.g., Gaussian. Resistance relates to the sensitivity of the estimator to changes in a small part of the data (termed outliers or flyers).

Graybill (1961) calls a model, where error exists in both the independent and dependent variables, a functional relationship. He solved two special cases. The first case is termed the controlled independent-variable model. It is the underlying model for solving Equation 7, when the assumption of high-precision ground-truth data being available is relaxed. The same least-squares estimator is used, but with larger confidence intervals. The second case exists when the ratio of the error variances are assumed to be constant. This case applies to

Equation 8 (for multiple-altitude data) and Equation 12 (for multiple-view-angle data). Standard least-squares estimates, calculated for this case, are biased. Appendix C shows the derivation for unbiased estimators of β_0 and β_1. The Graybill's modified least-squares regression method was implemented as a procedural change within SAS user statements. A sample SAS input is given in Appendix B. Using Graybill's regression method, a re-analysis was done of selected sets of aerial thermal sensor data from theses by Byrnes (1983) and Macleod (1984). The 1000 ft, 2000 ft, 4000 ft and 6000 ft altitude data from Byrnes and the Stirling and Simpson sites from Macleod were studied.

The use of least-squares regression in estimating parameters has much historical precedence. The errors in the dependent variable are often assumed to be independent and identically Gaussian distributed. Fortunately, least-squares regression is fairly robust. Unfortunately, it is not resistant; applied statisticians spend much effort in identifying and analyzing outliers. The magnitude of this problem can be seen with reference to regressions on Byrnes' 4000 ft altitude data set (total sample size of 11). Eliminating a single data point results in a 20% increase in the estimated nadir atmospheric transmittance [$\hat{\tau}(H,0)$ goes from 0.75 to 0.93] and an 85% decrease in the estimated nadir upwelled radiance [$\hat{L}_U(H,0)$ goes from 15.07 to 2.24 W m^{-2} sr^{-1}]. Larger sample sizes do help to minimize this problem however, as can be seen in a regression done on his 1000 ft altitude data set (total sample size of 34). In this case, elimination of two data points results in a 5% increase in the nadir atmospheric transmittance [$\hat{\tau}(H,0)$ changes from 0.84 to 0.88] and a 29% decrease in the nadir upwelled radiance [$\hat{L}_U(H,0)$ changes from 9.54 to 6.73 W m^{-2} sr^{-1}].

Within the past two decades, a resistant regression procedure has been developed (Mosteller and Tukey 1977). This procedure, termed "biweight regression" (shortened form of "bisquare-weight regression"), is essentially a weighted regression done iteratively, where low weight is given to observations having high residual values. Appendix D defines the equations for calculating the weights and the iteration procedure. This code was also implemented in SAS; Appendix B contains a sample input. The same data sets from Byrnes and Macleod were also analyzed using biweight regression.

Although trends existed in the re-analysis of the aerial sensor data, since there was no ground truth it could not be determined if they were going in the right direction. LOWTRAN 7 was therefore used to simulate data for analyzing the effects of different random noise levels, statistical estimation methods and sample sizes on the estimators β_0 and β_1. LOWTRAN was run to simulate 80 objects acquired using a broadband LWIR sensor through a midlatitude summer atmosphere at 4000 ft and view angles of 0° and 40°. Object temperatures were randomly selected from a uniform distribution with a mean equal to that of the Byrnes' data set (294.5 K) and a range of Macleod's Stirling data set (19.6 K). Object emissivities were randomly selected from a Gaussian distribution with a mean of 0.9 and a standard deviation of 0.005. Three levels of random noise were added to LOWTRAN produced radiances to analyze their effects: the first was none; the second was Gaussian noise with a mean of 0 and a standard deviation of 0.5 W m^{-2} sr^{-1} (approximately 1.5% of the average radiance); the third was 0 mean Gaussian noise with a standard deviation of 1.0 W m^{-2} sr^{-1} (3% noise) for 95% of the samples and 3.0 W

m^{-2} sr^{-1} (9% noise) for the remaining 5% of the samples. Estimates of β_0 and β_1 were computed using ordinary least squares, Graybill's method, Tukey's biweight method, and a combination of the Graybill and Tukey method (using the biweight approach to de-weighting outliers given a functional model). The effect of sample size on the estimators was analyzed using sub-samples of 10, 20 and 40 objects.

3.4 Error Propagation

To a first approximation, the error propagated through a given atmospheric correction technique can be estimated using the method of Beers (1957). For each step in an atmospheric correction technique, the contribution of the assumed independent errors on the output variable of that step can be written as

$$\hat{\sigma}_Y = \sqrt{ \sum_{n=1}^{N} \left[\frac{\partial Y}{\partial X_n} \hat{\sigma}_{X_n} \right]^2 } \qquad (40)$$

where $\hat{\sigma}$ is the estimated standard error, Y is the output variable of the step, X_n is the nth input variable, and N is the total number of input variables in the step.

An analysis of the relative magnitudes of the error components points to areas where increased sample size, alternate procedures, or alternate instrumentation may be used to improve the overall precision of an atmospheric correction technique. Appendix E gives the error propagation equations for the multiple-view-angle atmospheric correction technique. Analogous to Section 3.2, this computer code was originally written in Fortran and subsequently rewritten in C. The commented C source code is included in Appendix B.

4. RESULTS

The results of the enhancements to the multiple-view-angle technique are presented and discussed in Section 4.1. Section 4.2 gives the results of the new statistical estimators for both re-analyses of Byrnes' and Macleod's aerial sensor data sets and Monte Carlo simulations using known input data. Section 4.3 presents the results of an error propagation analysis for a multiple-view-angle atmospheric correction technique.

4.1 Multiple-view-angle Technique

The results of the model fits to the dependent data set (the LOWTRAN 7 midlatitude summer, tropical and subartic winter data) are given in Section 4.1.1. The results of selected model fits to the independent data sets are given in Section 4.1.2.

4.1.1 Regression Analyses on LOWTRAN 7 Data

The dependent data set was used to derive the coefficients for the atmospheric models given in Table 1. The results of regression analyses, which included a detailed examination of the residuals, is summarized in Table 3. The best model is Model 6, which can be re-written as

$$\tau(H, \theta) = \tau(H,0)^{[\sec \theta]^{\kappa}}, \tag{41}$$

where $\kappa = 0.61$ for a winter atmosphere (very clear conditions) and LWIR sensor, $\kappa = 0.79$ for all other conditions and LWIR sensor, or $\kappa = 0.34$ for all atmospheric conditions and MWIR sensor. Note that the simple secant atmospheric model, Equation 27 in Table 1, is a special case of

23

Equation 41 where $\kappa = 1.00$.

Table 3: Regression analyses of atmospheric transmittance models

Model	Sensor	R^2	Average | error |	Max error	Comment
1. Simple secant	LWIR	—	0.04	0.18	Poor model as $\hat{\tau}(H,\theta) \le \tau(H,\theta)$
	MWIR	—	0.11	0.37	
2. Optical depth	LWIR	91.0%	0.06	0.17	Poor model as residuals are
	MWIR	82.3%	0.09	–0.15	quadratic function of $\tau(H,\theta)$
3. Altitude and secant	LWIR	99.3%	0.06	0.17	Fair model, but largest errors
	MWIR	99.9%	0.01	0.04	at clearest atmospheres
4. Linear correction of secant	LWIR	98.2%	0.02	0.07	Fair model, but largest errors
	MWIR	97.6%	0.09	0.19	at clearest atmospheres
5. Multiplicative correction of secant	LWIR	99.4%	—	0.02	Good model, but β_0 term
	MWIR	99.2%	—	0.03	allows $\hat{\tau}(H,\theta) > \tau(H,0)$
6. Secant to power	LWIR	99.8%	0.003	0.02	Best model
	MWIR	99.7%	0.002	0.02	

A similar effort for the upwelled radiance models given in Table 2 is summarized in Table 4. Model 4 is the best model for LWIR data and Model 7 is best for MWIR data. They can be combined into the more general equation

$$L_U(H,\theta) = L_U(H,0) \left[\sec \theta\right]^{\kappa_1} \left[\frac{\tau(H,\theta)}{\tau(H,0)}\right]^{\kappa_2}, \tag{42}$$

where $\kappa_1 = 0.64$ and $\kappa_2 = 0$ for a LWIR sensor, $\kappa_1 = \kappa_2 = 0.47$ for winter atmosphere (very clear conditions) and MWIR sensor, or $\kappa_1 = \kappa_2 = 0.34$ for all other atmospheres and MWIR sensor. Note that the simple secant upwelled radiance model, Equation 33 in Table 2, is a special case of Equation 42 where $\kappa_1 = 1.00$ and $\kappa_2 = 0.00$. Also, note that Schott's model, Equation 34 in Table 2, is a special case of Equation 42 where $\kappa_1 = \kappa_2 = 1.00$.

Table 4: Regression analyses of upwelled radiance models

Model	Sensor	R^2	Ave |error| [W m^{-2} sr^{-1}]	Max error [W m^{-2} sr^{-1}]	Comment
1. Simple secant	LWIR	—	—	58.0	Poor model as
	MWIR	—	—	6.8	$\widehat{L_u}(H,\theta) \geq L_u(H,\theta)$
2. Schott's	LWIR	—	—	–25.0	Poor model for high θ
	MWIR	—	—	–1.9	
3. Byrnes'	LWIR	—	—	8.2	Poor model for high θ
	MWIR	—	—	5.6	
4. Secant to power	LWIR	99.1%	0.12	14.4	Best model for LWIR
	MWIR	96.8%	0.02	0.23	
5. Linear function of $\tau(H,\theta)$	LWIR	99.9%	0.39	2.9	Good model, but
	MWIR	98.4%	0.44	1.9	residuals $\propto H$
6. Linear function of Schott's	LWIR	85.1%	3.40	–19.2	Poor model for LWIR as
	MWIR	99.3%	0.14	0.25	residuals $\propto \theta$
7. Modified Schott's	LWIR	34.3%	0.83	–16.5	Best for MWIR
	MWIR	99.1%	0.004	–0.06	

The real worth of an atmospheric correction technique is usually measured with respect to its temperature prediction error. Given images at two view angles, one being at nadir, then the calculations described in Section 2.3 can be used for predicting the temperatures of objects. Table 5 summarizes the temperature prediction errors calculated using three atmospheric correction methods for a subset of the dependent data set. The first method, termed the secant method, uses the simple secant models (Equations 27 and 33). The second method, termed the Schott method, uses Equations 27 and 34. The third method, termed the revised method, uses Equations 41 and 42. Analogous to the derivation of Equation 16, the revised method gives

$$\widehat{\tau}(H,0) = \widehat{\beta}_1^{\,1/([\sec\theta]^\kappa - 1)} \tag{43}$$

$$\hat{\tau}(H,0) = \hat{\beta}_1^{\,1/([\sec\theta]^\kappa - 1)}.\tag{43}$$

Analogous to the derivation of Equation 20, the revised method gives

$$\hat{L}_U(H,0) = \frac{\hat{\beta}_0}{\hat{\beta}_1^{\,\kappa_2}[\sec\theta]^{\kappa_1} - \hat{\beta}_1}.\tag{44}$$

The dependent data subset included all four altitudes (1000 ft, 2000 ft, 4000 ft and 8000 ft), and the 20°, 40°, and 60° view angle data. The 80° view angle data, although necessary in the development of the revised atmospheric correction models, would not relate to large enough object images and was not used in the temperature prediction error statistics. No consistent trends in temperature prediction errors were found as a function of view angle, altitude or object temperature.

Table 5: Temperature prediction errors for dependent data set
(average absolute value [K])

Case	LWIR			MWIR		
	Secant	Schott	Revised	Secant	Schott	Revised
Midlatitude summer	1.7	2.3	0.8	6.8	6.9	1.1
Subartic winter	0.5	0.4	0.4	3.9	4.2	1.6
Tropical	3.8	5.4	2.1	7.9	7.4	1.2
Overall average	2.0	2.7	1.1	6.2	6.2	1.3

4.1.2 Analysis of Validation Data Sets

Analogous to the previous section, subsets of the five independent data sets (described in Section 3.1) were used to validate the atmospheric correction models and their regression-derived coefficients. Table 6 summarizes the results. Again, no consistent trends in temperature prediction errors were found as a function of view angle, altitude or

object temperature. In comparison to Table 5, a closer temperature prediction errors between the three methods for the LWIR data is evident; it is due to the offsetting biases in the secant and Schott models for estimating $\hat{\tau}(H,0)$ and $\hat{L}_U(H,0)$ at the specified temperatures. This is illustrated in Figures 8 and 9 for the data set with the largest average error.

Table 6: Temperature prediction errors for validation data set (average absolute value [K])

Case	LWIR			MWIR		
	Secant	Schott	Revised	Secant	Schott	Revised
Midlatitude (ε=0.986)	1.2	2.5	0.9	6.4	7.4	1.0
20 Jun 84 radiosonde	1.1	1.9	1.7	6.4	6.3	1.2
22 Jun 84 radiosonde	0.8	0.8	0.9	5.7	6.1	1.3
6 Oct 84 radiosonde	1.1	1.3	0.3	>19.9	>19.9	0.6
24 Feb 87 radiosonde	1.3	1.3	0.4	10.2	10.6	0.9
Overall average	1.1	1.6	0.8	>9.7	>10.1	1.0

Figure 8: Predicted vs actual LWIR transmittance (20 June 1984 radiosonde data, 0°/60° view angles)

Figure 9: Predicted vs actual upwelled LWIR radiance (20 June 1984 radiosonde data, 0°/60° view angles)
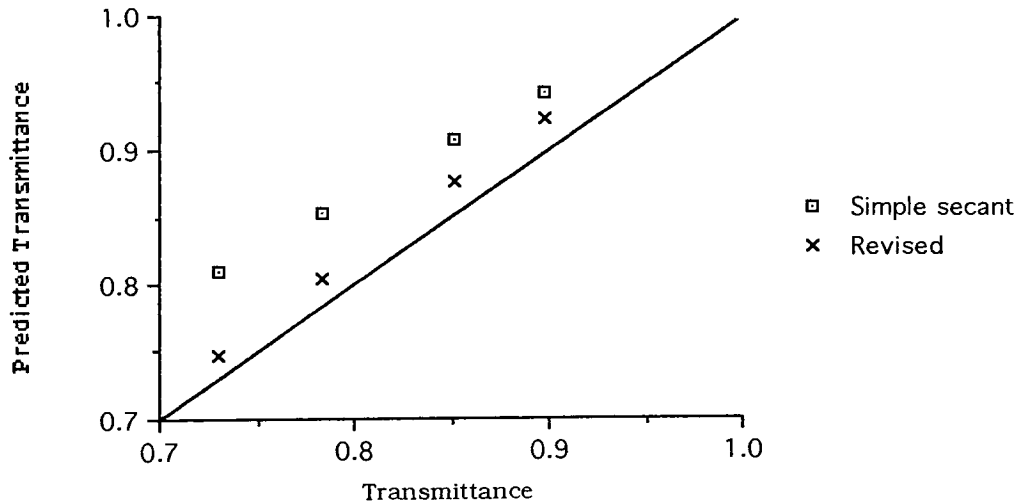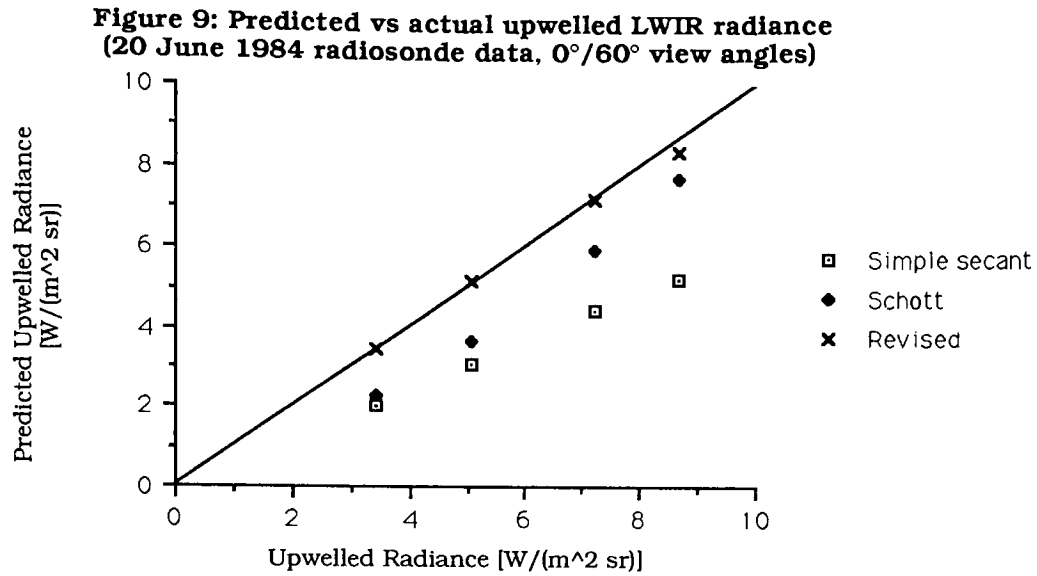
4.2 Statistical Estimation

Although significant time was spent in re-analyzing the data sets of Byrnes (1983) and Macleod (1984), as stated in Section 3.3 it is unclear whether the trends are significant because there was no ground truth. Therefore, only two illustrative examples will be given. Using Byrnes' 4000 ft altitude data set, a functional relationship solution gives a 4% increase in the predicted nadir atmospheric transmittance [the estimate of $\tau(H,0)$ changes from 0.75 to 0.78] and an 18% decrease in the predicted nadir upwelled radiance [the estimate of $L_U(H,0)$ changes from 15.07 to 12.39 W m^{-2} sr^{-1}]. Applying biweight regression to the same data set, gives an estimated nadir atmospheric transmittance of 0.88 [a 17% increase] and an estimated nadir upwelled radiance of 5.92 W m^{-2} sr^{-1} (a 61% decrease). The estimates from both the functional and biweight regressions are closer to the values of Byrnes' "independent

28

agent" (Professor John Schott) than those given by a least-squares fit to either the original data set or a data set with removal of a single outlier.

Analysis of the regressions done by ordinary least squares, functional model, biweight, and biweighted functional model on the simulation data showed no significant difference in the estimates for β_1 and consequently for $\tau(H,0)$. The range of $\hat{\beta}_1$ is 0.93–0.97 ($\beta_1 = 0.93$). The estimates for β_0 are significantly different, as can be seen in Table 7. Adding random noise to the raw data decreases $\hat{\beta}_0$, with both the biweight and biweighted function estimators being better for the mixed noise case; they are therefore more robust estimators. Both the ordinary-least-squares and functional-model estimators show a significant trend in lower values for smaller sample sizes. The biweight and biweighted function estimators, on the other hand, are less affected and therefore more resistant, down to a sample size of 20. Converting these regression coefficient errors to temperature errors gives a positive bias of 0.24–0.80 K for ordinary least squares and 0.13–0.53 K for biweight regression, given an object at 295 K.

Table 7: $\hat{\beta}_0$ from simulation of multiple-view-angle imagery
(4000 ft, 0° and 40° views, midlatitude summer, $\beta_0 = 2.22$)

Case	Least squares	Functional	Biweight	Biweighted functional
1. $\sigma = 0.5 \text{ W m}^{-2} \text{ sr}^{-1}$, 80 samples	2.18	2.17	2.17	2.17
2. $\sigma = 1.0$ for 95% of data, $\sigma = 3.0$ for 5%. 80 samples	1.72	1.71	1.97	1.96
3. Case 2, 40 samples	1.80	1.78	1.98	1.96
4. Case 2, 20 samples	1.54	1.52	1.90	1.89
5. Case 2, 10 samples	1.18	1.16	0.97	0.96

4.3 Error Propagation

Using the error propagation approach discussed in Section 3.4 and detailed in Appendix E, the effects of various factors were studied. Table 8 lists the input data used for the analysis, their associated root-mean-square (rms) errors (the standard errors), and a reference.

Table 8: Error propagation input data

Source	Value	rms error	Reference
Film density [d]	0.35, 0.59, 0.86, 1.09, 1.24, 1.33, 1.44, 1.52	0.01, 0.01, 0.005, 0.005, 0.005, 0.005, 0.005, 0.01	Macleod (p. 69)
Sensor voltage [V]	0.0, 1.0, 2.0, 3.0, 4.0, 5.0, 6.0, 7.0	derived via Equation E2	Macleod (p. 69)
Blackbody voltage [V]	3.733	equivalent to rms sensor voltage	Macleod (p. 69) with correction
Sensor gain	2.434	0.097	Byrnes (p. 103) & Schott (2Apr90)
Blackbody Temperature [K]	295.15	0.112	Byrnes (p.142 & p.115)
Downwell radiance [$W\,m^{-2}\,sr^{-1}$]	9.92	0.99	typical values (Schott 2Apr90)
Object emissivity	0.90	0.005	Schott (2Apr90)
Regression slope (β_1)	computed	0.10 x computed value	typical value for 20 samples & biweight
Regression intercept (β_0)	computed	0.008 x computed value	typical value for 20 samples & biweight

One of the factors studied was regression estimators for the revised multiple-view-angle technique. Table 9 summarizes the results. Use of the biweight regression estimators result in significantly smaller overall random error than least-squares. Any improvement due to increased sample size is probably not realizable, e.g., consider the difficulty of identifying 80 objects of different radiance levels in two different view angle images.

Table 9: Total random (rms) error for multiple-view-angle technique [K]
(0° and 40° views, midlatitude summer, 300 K object)

Case	1000 ft	2000 ft	4000 ft	8000 ft
1. 3% noise for 95% of data, 9% noise for 5% of data, 20 samples, least squares estimators	2.7	3.3	4.2	5.0
2. Case 1, 20 samples, biweight estimators	2.0	2.3	2.8	3.3
3. Case 1, 40 samples, biweight estimators	1.7	1.9	2.3	2.7
4. Case 1, 80 samples, biweight estimators	1.0	1.2	1.4	1.6

Table 10 presents an analysis of the total random error associated with the major error sources. Note that, in all cases, the atmospheric transmittance and upwelled radiance estimators account for most of random temperature error. Also, note that the dominant component between the two changes as a function of view angle.

Table 10: Error components for multiple-view-angle technique [%]
(4000 ft, midlatitude summer, 300 K object, 20 samples, mixed noise model)

Error component	20°	40°	60°
$\hat{\tau}(H,0)$	93.4	39.8	6.4
$\hat{L}_u(H,0)$	5.5	49.5	79.9
Emissivity	0.4	4.1	6.2
Downwell radiance	0.1	1.3	2.2
Density	0.2	1.9	1.1
Sensor gain	<0.1	0.1	0.9

5. CONCLUSIONS AND RECOMMENDATIONS

5.1 Conclusions

1. Using the LOWTRAN radiative transfer model as truth, a revised multiple-view-angle atmospheric correction technique has been developed and tested for night-time thermal infrared imaging. Its average absolute temperature prediction accuracy for an independent data set is 0.8 K for LWIR and 1.0 K for MWIR.

2. The effect of measurement errors on the estimates of atmospheric transmittance and upwelled radiance are significant, especially for sample sizes smaller than 20. For the cases analyzed, a positive bias of 0.24–0.80 K, relative to an object at 295 K, was found. The use of the robust and resistant regression algorithm, Tukey's biweight, reduced the effect; the positive bias was reduced to 0.13–0.53 K.

3. An end-to-end error propagation computer program was developed for the revised multiple-view-angle atmospheric correction technique. Running it with real-world values for the error components, resulted in a total rms error of 1.0–3.3 K. The regression coefficients, and consequently the atmospheric transmittance and upwelled radiance estimators, are the most significant contributors; they account for greater than 86% of the total rms error.

5.2 Recommendations

1. The foremost recommendation is to validate this revised multiple-view-

angle atmospheric correction technique with real aerial remote sensing data. Ground truth is mandatory for the collections.

2. Given multiple-view-angle images of the same objects, investigate the benefit of pooling the estimates of $\tau(H,0)$ and $L_U(H,0)$ from the various pair-wise multiple regressions.

3. If the revised multiple-view-angle atmospheric correction technique is validated, compare it to the multiple-altitude technique. The myriad combinations of altitudes, view angles, time delays between flights and LOWTRAN standard atmospheres suggest that this comparison be done on a real-world case-by-case basis rather than via simulation.

4. Investigate a "profile" approach using multiple-view-angle data. Given multiple-view-angle images of the same objects, regress $\{L(H,\theta_k)\}$ on the error-free $\{\theta_k\}$ for each ith object. With large enough sample sizes and a simple (first-order or second-order) linear relationship, the resultant intercepts may be good estimates of $\{L_i(H,0)\}$. A subsequent regression of $\{L_i(H,\theta_k)\}$ on $\{\widehat{L_i}(H,0)\}$ will then estimate β_0 and β_1, and consequently estimate τ and L_U.

Appendix A – LOWTRAN Data Sets

Table A1: LWIR dependent data set [W/(m^2 sr)]

Atmosphere	Altitude	View Angle	Object Temperature			
			284 K	290 K	295 K	315 K
midlat summer	1000 ft	0°	29.011	31.614	33.905	44.207
		20°	29.051	31.639	33.917	44.156
		40°	29.199	31.729	33.958	43.975
		60°	29.576	31.961	34.061	43.502
		80°	31.037	32.848	34.444	41.627
	2000 ft	0°	29.429	31.847	33.976	43.546
		20°	29.487	31.881	33.990	43.467
		40°	29.694	32.004	34.039	43.188
		60°	30.216	32.313	34.161	42.472
		80°	32.047	33.382	34.560	39.864
	4000 ft	0°	29.774	31.963	33.891	42.559
		20°	29.844	32.001	33.901	42.442
		40°	30.091	32.134	33.933	42.028
		60°	30.688	32.451	34.005	41.000
		80°	32.482	33.362	34.138	37.640
	8000 ft	0°	29.765	31.747	33.493	41.347
		20°	29.830	31.773	33.485	41.187
		40°	30.054	31.862	33.455	40.621
		60°	30.564	32.049	33.357	39.250
		80°	31.718	32.297	32.808	35.116
tropical	1000 ft	0°	29.798	32.289	34.482	44.344
		20°	29.875	32.345	34.520	44.298
		40°	30.149	32.544	34.653	44.135
		60°	30.851	33.052	34.992	43.714
		80°	33.437	34.921	36.230	42.125
	2000 ft	0°	30.557	32.803	34.782	43.682
		20°	30.664	32.879	34.831	43.609
		40°	31.041	33.148	35.003	43.351
		60°	31.969	33.806	35.424	42.709
		80°	34.951	35.910	36.756	40.575
	4000 ft	0°	31.181	33.121	34.831	42.524
		20°	31.304	33.203	34.877	42.408
		40°	31.734	33.490	35.037	42.002
		60°	32.734	34.151	35.400	41.028
		80°	35.235	35.746	36.197	38.239
	8000 ft	0°	31.257	32.907	34.361	40.910
		20°	31.369	32.970	34.382	40.738
		40°	31.746	33.180	34.445	40.144
		60°	32.534	33.597	34.535	38.765
		80°	33.735	33.988	34.212	35.227
			250 K	265 K	270 K	280 K
artic winter	1000 ft	0°	14.718	19.763	21.671	25.838
		20°	14.724	19.762	21.667	25.827
		40°	14.745	19.756	21.651	25.789
		60°	14.795	19.738	21.607	25.688
		80°	14.972	19.643	21.410	25.268
	2000 ft	0°	14.801	19.750	21.621	25.708
		20°	14.809	19.747	21.614	25.692
		40°	14.840	19.738	21.590	25.635
		60°	14.914	19.709	21.523	25.484
		80°	15.166	19.558	21.219	24.846
	4000 ft	0°	14.911	19.728	21.549	25.527
		20°	14.924	19.724	21.540	25.504
		40°	14.968	19.710	21.503	25.420
		60°	15.071	19.666	21.403	25.198
		80°	15.412	19.430	20.949	24.267
	8000 ft	0°	14.979	19.642	21.406	25.257
		20°	14.993	19.635	21.390	25.224
		40°	15.043	19.607	21.333	25.102
		60°	15.159	19.526	21.178	24.785
		80°	15.524	19.132	20.497	23.476

Table A2: MWIR dependent data set [W/(m^2 sr)]

Atmosphere	Altitude	View Angle	Object Temperature			
			284 K	290 K	295 K	315 K
midlat summer	1000 ft	0°	1.725	1.896	2.066	3.058
		20°	1.732	1.900	2.067	3.045
		40°	1.753	1.913	2.071	3.001
		60°	1.798	1.939	2.079	2.905
		80°	1.908	2.003	2.098	2.662
	2000 ft	0°	1.762	1.907	2.050	2.893
		20°	1.769	1.910	2.051	2.879
		40°	1.789	1.922	2.053	2.831
		60°	1.831	1.945	2.059	2.731
		80°	1.931	1.999	2.069	2.483
	4000 ft	0°	1.705	1.825	1.944	2.649
		20°	1.709	1.826	1.943	2.633
		40°	1.723	1.831	1.939	2.578
		60°	1.751	1.840	1.930	2.463
		80°	1.809	1.856	1.904	2.192
	8000 ft	0°	1.548	1.649	1.749	2.345
		20°	1.550	1.648	1.745	2.326
		40°	1.554	1.643	1.732	2.262
		60°	1.561	1.632	1.703	2.130
		80°	1.565	1.597	1.630	1.828
tropical	1000 ft	0°	1.969	2.128	2.287	3.217
		20°	1.978	2.135	2.291	3.207
		40°	2.011	2.159	2.306	3.173
		60°	2.078	2.208	2.337	3.101
		80°	2.243	2.328	2.412	2.919
	2000 ft	0°	2.020	2.153	2.285	3.064
		20°	2.029	2.159	2.289	3.053
		40°	2.059	2.181	2.301	3.016
		60°	2.122	2.225	2.328	2.938
		80°	2.268	2.328	2.388	2.749
	4000 ft	0°	1.914	2.022	2.130	2.770
		20°	1.920	2.026	2.131	2.756
		40°	1.940	2.037	2.134	2.709
		60°	1.980	2.059	2.138	2.611
		80°	2.061	2.100	2.140	2.382
	8000 ft	0°	1.712	1.800	1.889	2.417
		20°	1.714	1.800	1.886	2.400
		40°	1.723	1.800	1.878	2.342
		60°	1.737	1.798	1.859	2.225
		80°	1.753	1.779	1.804	1.962
			250 K	265 K	270 K	280 K
subartic winter	1000 ft	0°	0.389	0.622	0.734	1.023
		20°	0.391	0.622	0.732	1.019
		40°	0.395	0.619	0.726	1.005
		60°	0.406	0.614	0.713	0.972
		80°	0.436	0.597	0.674	0.876
	2000 ft	0°	0.406	0.615	0.715	0.976
		20°	0.407	0.614	0.713	0.971
		40°	0.413	0.611	0.706	0.954
		60°	0.425	0.605	0.691	0.915
		80°	0.458	0.586	0.647	0.809
	4000 ft	0°	0.423	0.606	0.693	0.922
		20°	0.425	0.605	0.691	0.916
		40°	0.431	0.601	0.683	0.897
		60°	0.444	0.594	0.666	0.855
		80°	0.477	0.573	0.620	0.743
	8000 ft	0°	0.412	0.570	0.647	0.846
		20°	0.414	0.569	0.644	0.839
		40°	0.418	0.563	0.633	0.817
		60°	0.427	0.551	0.611	0.768
		80°	0.447	0.518	0.553	0.644

Table A3: LWIR independent data set [W/(m^2 sr)]

Case	Altitude	View Angle	Object Temperature			
			284 K	290 K	295 K	315 K
#1-midlatitude summer emissivity=0.986	1000 ft	0°	31.256	34.098	36.600	47.839
		20°	31.282	34.107	36.594	47.767
		40°	31.377	34.140	36.573	47.506
		60°	31.619	34.224	36.518	46.828
		80°	32.550	34.531	36.276	44.130
	2000 ft	0°	31.504	34.145	36.470	46.919
		20°	31.540	34.156	36.458	46.808
		40°	31.670	34.194	36.417	46.410
		60°	31.995	34.288	36.308	45.390
		80°	33.132	34.593	35.882	41.687
	4000 ft	0°	31.643	34.035	36.142	45.614
		20°	31.684	34.041	36.117	45.451
		40°	31.827	34.060	36.028	44.875
		60°	32.169	34.099	35.798	43.448
		80°	33.170	34.134	34.984	38.819
	8000 ft	0°	31.453	33.620	35.530	44.116
		20°	31.483	33.608	35.480	43.900
		40°	31.584	33.562	35.304	43.142
		60°	31.803	33.428	34.861	41.309
		80°	32.153	32.787	33.347	35.876
#2-radiosonde data 20 June 1984	1000 ft	0°	28.564	31.217	33.552	44.036
		20°	28.602	31.244	33.569	44.009
		40°	28.734	31.337	33.628	43.916
		60°	29.077	31.578	33.780	43.668
		80°	30.441	32.527	34.365	42.625
	2000 ft	0°	28.894	31.414	33.630	43.582
		20°	28.948	31.449	33.650	43.536
		40°	29.131	31.571	33.720	43.370
		60°	29.594	31.879	33.892	42.935
		80°	31.318	33.005	34.491	41.179
	4000 ft	0°	29.144	31.457	33.493	42.642
		20°	29.204	31.491	33.505	42.555
		40°	29.417	31.613	33.548	42.243
		60°	29.934	31.904	33.638	41.440
		80°	31.575	32.749	33.784	38.450
	8000 ft	0°	29.107	31.262	33.161	41.696
		20°	29.162	31.287	33.158	41.570
		40°	29.355	31.369	33.143	41.121
		60°	29.802	31.543	33.078	39.985
		80°	30.923	31.791	32.557	36.015
#3-radiosonde data 22 June 1984	1000 ft	0°	28.514	31.249	33.657	44.480
		20°	28.532	31.257	33.657	44.443
		40°	28.597	31.287	33.657	44.307
		60°	28.763	31.365	33.657	43.958
		80°	29.432	31.678	33.657	42.558
	2000 ft	0°	28.780	31.390	33.689	44.022
		20°	28.809	31.404	33.690	43.966
		40°	28.912	31.455	33.695	43.763
		60°	29.177	31.585	33.706	43.245
		80°	30.200	32.088	33.751	41.239
	4000 ft	0°	28.991	31.449	33.613	43.345
		20°	29.028	31.465	33.611	43.263
		40°	29.160	31.523	33.605	42.966
		60°	29.492	31.670	33.588	42.217
		80°	30.690	32.190	33.512	39.469
	8000 ft	0°	28.792	31.123	33.176	42.409
		20°	28.821	31.126	33.157	42.292
		40°	28.921	31.138	33.090	41.873
		60°	29.168	31.163	32.921	40.831
		80°	29.944	31.172	32.256	37.141

Table A3 (con't): LWIR independent data set [W/(m^2 sr)]

Case	Altitude	View Angle	Object Temperature			
			284 K	290 K	295 K	315 K
#4-radiosonde	1000 ft	0°	27.697	30.462	32.895	43.817
data		20°	27.697	30.456	32.884	43.784
6 October 1984		40°	27.697	30.435	32.845	43.665
		60°	27.692	30.378	32.741	43.354
		80°	27.642	30.112	32.286	42.052
	2000 ft	0°	27.654	30.347	32.718	43.361
		20°	27.652	30.337	32.699	43.309
		40°	27.644	30.297	32.633	43.120
		60°	27.616	30.189	32.454	42.627
		80°	27.453	29.701	31.681	40.577
	4000 ft	0°	27.627	30.275	32.606	43.073
		20°	27.623	30.260	32.582	43.009
		40°	27.606	30.206	32.495	42.777
		60°	27.551	30.056	32.262	42.172
		80°	27.235	29.358	31.228	39.632
	8000 ft	0°	27.533	30.121	32.399	42.633
		20°	27.525	30.100	32.367	42.553
		40°	27.494	30.025	32.253	42.263
		60°	27.403	29.820	31.948	41.511
		80°	26.935	28.899	30.630	38.408
#5-radiosonde	1000 ft	0°	27.563	30.370	32.841	43.931
data		20°	27.558	30.361	32.828	43.903
24 February 1987		40°	27.539	30.328	32.783	43.804
		60°	27.485	30.238	32.662	43.542
		80°	27.234	29.839	32.132	42.431
	2000 ft	0°	27.481	30.242	32.672	43.583
		20°	27.472	30.227	32.652	43.541
		40°	27.439	30.174	32.581	43.391
		60°	27.349	30.032	32.393	42.996
		80°	26.940	29.414	31.592	41.376
	4000 ft	0°	27.348	30.060	32.447	43.167
		20°	27.334	30.038	32.418	43.108
		40°	27.280	29.957	32.313	42.896
		60°	27.133	29.740	32.036	42.347
		80°	26.458	28.784	30.832	40.034
	8000 ft	0°	27.181	29.843	32.187	42.714
		20°	27.160	29.813	32.148	42.638
		40°	27.083	29.703	32.009	42.369
		60°	26.876	29.410	31.642	41.669
		80°	25.956	28.154	30.089	38.788

Table A4: MWIR independent data set [W/(m^2 sr)]

Case	Altitude	View Angle	Object Temperature			
			284 K	290 K	295 K	315 K
#1–midlatitude summer emissivity=0.986	1000 ft	0°	1.830	2.029	2.225	3.377
		20°	1.835	2.030	2.224	3.359
		40°	1.851	2.036	2.220	3.298
		60°	1.884	2.047	2.210	3.168
		80°	1.965	2.075	2.185	2.840
	2000 ft	0°	1.850	2.018	2.184	3.162
		20°	1.855	2.019	2.182	3.143
		40°	1.869	2.023	2.176	3.079
		60°	1.900	2.032	2.164	2.943
		80°	1.972	2.052	2.132	2.612
	4000 ft	0°	1.777	1.916	2.055	2.873
		20°	1.780	1.916	2.051	2.851
		40°	1.788	1.914	2.039	2.780
		60°	1.805	1.909	2.012	2.631
		80°	1.837	1.892	1.948	2.282
	8000 ft	0°	1.609	1.725	1.842	2.533
		20°	1.608	1.722	1.835	2.508
		40°	1.607	1.710	1.814	2.428
		60°	1.603	1.686	1.768	2.263
		80°	1.584	1.622	1.659	1.890
#2–radiosonde data 20 June 1984	1000 ft	0°	1.830	2.014	2.197	3.263
		20°	1.838	2.020	2.200	3.253
		40°	1.865	2.039	2.211	3.220
		60°	1.921	2.078	2.234	3.148
		80°	2.060	2.174	2.288	2.961
	2000 ft	0°	1.815	1.974	2.132	3.060
		20°	1.821	1.978	2.134	3.048
		40°	1.843	1.992	2.139	3.008
		60°	1.888	2.020	2.150	2.922
		80°	1.999	2.086	2.174	2.698
	4000 ft	0°	1.683	1.819	1.953	2.746
		20°	1.687	1.820	1.952	2.730
		40°	1.700	1.824	1.948	2.679
		60°	1.725	1.832	1.938	2.570
		80°	1.783	1.846	1.909	2.290
	8000 ft	0°	1.543	1.663	1.782	2.489
		20°	1.544	1.662	1.779	2.471
		40°	1.549	1.658	1.767	2.410
		60°	1.559	1.650	1.741	2.282
		80°	1.573	1.621	1.669	1.959
#3–radiosonde data 22 June 1984	1000 ft	0°	1.554	1.746	1.937	3.046
		20°	1.558	1.748	1.936	3.032
		40°	1.571	1.753	1.933	2.985
		60°	1.599	1.763	1.926	2.884
		80°	1.666	1.787	1.908	2.622
	2000 ft	0°	1.611	1.777	1.941	2.906
		20°	1.615	1.778	1.940	2.891
		40°	1.629	1.784	1.938	2.843
		60°	1.658	1.795	1.932	2.739
		80°	1.729	1.822	1.915	2.471
	4000 ft	0°	1.594	1.737	1.879	2.713
		20°	1.597	1.737	1.877	2.697
		40°	1.608	1.740	1.871	2.644
		60°	1.631	1.745	1.858	2.531
		80°	1.683	1.753	1.822	2.238
	8000 ft	0°	1.379	1.505	1.630	2.371
		20°	1.378	1.501	1.624	2.350
		40°	1.376	1.491	1.605	2.283
		60°	1.371	1.468	1.564	2.138
		80°	1.349	1.401	1.454	1.771

Table A4 (con't): MWIR independent data set [W/(m^2 sr)

Case	Altitude	View Angle	Object Temperature			
			284 K	290 K	295 K	315 K
#4–radiosonde data 6 October 1984	1000 ft	0°	1.282	1.535	1.784	3.225
		20°	1.280	1.531	1.778	3.208
		40°	1.271	1.515	1.755	3.147
		60°	1.250	1.478	1.704	3.009
		80°	1.189	1.371	1.551	2.601
	2000 ft	0°	1.237	1.469	1.698	3.024
		20°	1.233	1.463	1.689	3.002
		40°	1.222	1.443	1.662	2.931
		60°	1.196	1.399	1.600	2.770
		80°	1.122	1.276	1.429	2.323
	4000 ft	0°	1.175	1.392	1.605	2.845
		20°	1.171	1.384	1.595	2.821
		40°	1.155	1.360	1.563	2.740
		60°	1.121	1.306	1.490	2.560
		80°	1.021	1.152	1.282	2.049
	8000 ft	0°	1.105	1.306	1.505	2.662
		20°	1.099	1.297	1.494	2.635
		40°	1.079	1.268	1.455	2.544
		60°	1.034	1.202	1.369	2.341
		80°	0.907	1.018	1.128	1.776
#5–radiosonde data 24 February 1987	1000 ft	0°	1.368	1.597	1.822	3.132
		20°	1.368	1.594	1.817	3.114
		40°	1.365	1.583	1.798	3.051
		60°	1.359	1.560	1.758	2.915
		80°	1.342	1.496	1.649	2.548
	2000 ft	0°	1.317	1.520	1.721	2.893
		20°	1.315	1.516	1.714	2.871
		40°	1.310	1.501	1.691	2.800
		60°	1.296	1.470	1.641	2.647
		80°	1.259	1.384	1.507	2.239
	4000 ft	0°	1.311	1.503	1.694	2.805
		20°	1.309	1.499	1.686	2.783
		40°	1.303	1.483	1.662	2.708
		60°	1.289	1.450	1.610	2.546
		80°	1.249	1.357	1.466	2.107
	8000 ft	0°	1.245	1.423	1.599	2.629
		20°	1.242	1.417	1.591	2.605
		40°	1.232	1.397	1.561	2.522
		60°	1.209	1.354	1.498	2.342
		80°	1.144	1.234	1.324	1.857

Appendix B – Annotated Computer Program

```
/*****
 *
 * Calculates temperature prediction errors for a nadir image using
 * the revised multiple-view-angle atmospheric correction technique.
 * Written by Robert Mericsko.
 *
 *****/


#include <stdio.h>
#include <math.h>

main() {
    FILE  *in;                  // INPUT CASE FILE
    FILE  *radTempLUT;          // RADIANCE-TO-TEMPERATURE LOOK-UP TABLE
    FILE  *radInput;            // INPUT RADIANCE FILE (AT IMAGE PLANE)
    FILE  *out;                 // OUTPUT CASE FILE

    char  caseName[20];         // INPUT CASE FILENAME
    char  radName[20];          // INPUT RADIANCE FILENAME
    char  LUTname[20];          // RADIANCE-TO-TEMPERATURE LOOK-UP TABLE NAME
    char  outputName[20];       // OUTPUT CASE FILENAME

    float TLtable[40][2];       // TEMPERATURE-TO-RADIANCE LOOK-UP TABLE VALUES

    /*** CASE DATA ***/
    float voltage[8];           // SENSOR'S VOLTAGE CALIBRATION (TO DENSITY) VALUES
    float density[8];           // SENSOR'S DENSITY CALIBRATION (TO VOLTAGE) VALUES
    float se_density[8];        // STANDARD ERROR (RMS ERROR) OF DENSITY VALUES
    float emiss, se_emiss;      // EMISSIVITY AND ITS STANDARD ERROR
    float winterFlag;           // FLAG FOR WINTER (VERY CLEAR) ATMOSPHERE (0=NO, 1=YES)
    float IRflag;               // FLAG FOR INRARED BAND (0=MWIR, 1=LWIR)
    float beta1_tol, beta0_tol; // PROPORTIONAL ERRORS FOR REGRESSION ESTIMATORS
    float gain, se_gain;        // SENSOR'S GAIN AND ITS STANDARD ERROR
    float voltageBB;            // CALIBRATION BLACKBODY'S VOLTAGE
    float TBB, se_TBB;          // CALIBRATION BLACKBODY'S TEMPERATURE AND STANDARD ERROR
    float Ld, se_Ld;            // DOWNWELL RADIANCE AND ITS STANDARD ERROR


    /*** RADIANCE FILE DATA ***/
    float height, view;         // SENSOR'S ALTITUDE AND VIEW ANGLE
    float T[2];                 // BLACKBODY TEMPERATURES OF 2 OBJECTS
    float Lh0[2], LhTheta[2];   // RADIANCES AT SENSOR OF 2 OBJECTS
                                // (NADIR AND OFF-NADIR VIEWS)


    /*** OUTPUT VARIABLES ***/
    float Tout, se_Tout; // APPARENT OBJECT BLACKBODY TEMPERATURE AND ITS STANDARD
                         // ERROR ASSOCIATED WITH A SENSOR VOLTAGE CALIBRATION VALUE
    float trans_cont; // PERCENTAGE OF TEMPERATURE ERROR ASSOCIATED WITH ATMOSPHERIC
                      // TRANSMITTANCE ESTIMATION
    float Lu_cont;    // SAME FOR UPWELLED RADIANCE ESTIMATION
    float emiss_cont; // SAME FOR OBJECT EMISSIVITY STANDARD ERROR
    float Ld_cont;    // SAME FOR DOWNWELLED RADIANCE STANDARD ERROR
    float D_cont;     // SAME FOR DENSITY STANDARD ERROR
    float G_cont;     // SAME FOR SENSOR GAIN STANDARD ERROR
    float Tbb_cont;   // SAME FOR CALIBRATION BLACKBODY TEMPERATURE STANDARD ERROR

    /*** ATMOSPHERIC CORRECTION MODEL COEFFICIENTS ***/
    float kappa, kappa1, kappa2;

    /*** COUNTER VARIABLES ***/
```

```
int i=0;      // TEMPERATURE INDEX
int m;        // BREAKPOINTS IN CASE VOLTAGE AND DENSITY CASE DATA

/*** INTERMEDIATE VARIABLES ***/
int j=0, k, dummy;
float beta0, beta1, D_term, emiss_term, gamma, G_term, L0, L00[2], L00est,
      L0_cont, L0_term, Ld_term, Lsensor[8], Lsensor_cont, Lsensor_term,
      LT, Lt, LuH0, LuH0est, Lu_term, mess, p, se_beta0, se_beta1, secView,
      se_L0, se_Lsensor, se_LT, se_LuH0est, se_theta, se_transH0est, se_Tsensor,
      se_voltage, se_voltageBB, sumCos=0, sumRev1=0, sumRev2=0, sumSchott=0,
      sumX, sumX2, sumXY, sumY, Tbb_term, temp, tempEst, tError[4], Tsensor[8],
      transH0, transH0est, trans_term, X, Vbb_term;

/*** ASSIGN FILENAMES ***/
printf("Enter input case filename (e.g., :lwir:case1):   ");
scanf("%s",caseName);
if ( (in = fopen(caseName, "r") ) == NULL )
    printf("\nERROR   Cannot open the designated file\n");

printf("Enter input radiance filename (e.g., :lwir:midlat):   ");
scanf("%s",radName);
if ( (radInput = fopen(radName, "r") ) == NULL )
    printf("\nERROR - Cannot open the designated file\n");

printf("Enter filename for radiance-to-temperature look-up table");
printf("\n   (e.g., :lwir:radTemp):   ");
scanf("%s",LUTname);
if ( (radTempLUT = fopen(LUTname, "r") ) == NULL )
    printf("\nERROR - Cannot open the designated file\n");

printf("Enter output filename (e.g., :lwir:case1_out):   ");
scanf("%s",outputName);
out = fopen(outputName, "w");

/*** READ INPUT CASE DATA   ***/
fscanf( in, "%f%f%f%f%f%f%f%f", &voltage[0],&voltage[1],&voltage[2],
    &voltage[3],&voltage[4],&voltage[5],&voltage[6],&voltage[7]);
fscanf( in, "%f%f%f%f%f%f%f%f", &density[0],&density[1],&density[2],
    &density[3],&density[4],&density[5],&density[6],&density[7]);
fscanf( in, "%f%f%f%f%f%f%f%f", &se_density[0],&se_density[1],&se_density[2],
    &se_density[3],&se_density[4],&se_density[5],&se_density[6],&se_density[7]);
fscanf( in, "%f%f%f%f", &emiss, &se_emiss, &winterFlag, &IRflag);
fscanf( in, "%f%f", &beta0_tol, &beta1_tol);
fscanf( in, "%f%f", &gain, &se_gain);
fscanf( in, "%f%f%f", &voltageBB, &TBB, &se_TBB);
fscanf( in, "%f%f", &Ld, &se_Ld);

/*** READ IN RADIANCE-TO-TEMPERATURE TABLE ***/
for (j=0; j<40; j++) {
    fscanf( radTempLUT, "%f %d", &TLtable[j][0], &dummy );
    TLtable[j][1] = dummy;
    }

/*** SET ATMOSPHERIC-CORRECTION MODEL CONSTANTS ***/
if ( IRflag == 0 ) {    // MWIR DATA
    kappa = 0.34;
    if ( winterFlag == 0 )  kappa1 = kappa2 = 0.34;
    if ( winterFlag == 1 )  kappa1 = kappa2 = 0.47;
    }
if ( IRflag == 1 ) {    // LWIR DATA
    kappa1 = 0.64;
```

41

ErrProp.
Sunday, July 12, 1992 9:42 PM

Page 3

```
        kappa2 = 0;
        if ( winterFlag == 0 ) kappa = 0.79;
        if ( winterFlag == 1 ) kappa = 0.61;
        }


/*** REPEAT FOR EACH ALTITUDE'S DATA SET ***/
do {
    /*** READ IN NADIR DATA ***/
    for (i=0; i<2; i++) {
        fscanf(radInput, "%f%f%f%f", &height, &view, &T[i], &Lh0[i]);
        /*** COMPUTE L(0,0) FOR TWO TEMPERATURES SPECIFIED IN RADIANCE FILE***/
        for (j=0; j<40; j++) {
            if (T[i] == TLtable[j][1]) {
                L00[i] = TLtable[j][0] * emiss;
                break;
                }
            }
        }
    /*** CALCULATE TRUE NADIR TRANSMITTANCE AND UPWELLED RADIANCE ***/
    sumX = sumX2 = sumY = sumXY = 0;
    for (i=0; i<2; i++) {
        sumX = sumX + L00[i];
        sumX2 = sumX2 + L00[i] * L00[i];
        sumY = sumY + Lh0[i];
        sumXY = sumXY + L00[i] * Lh0[i];
        }
    transH0 = (sumY/2 * sumX - sumXY) / (sumX/2 * sumX   sumX2);
    LuH0 = (sumXY - sumY/2*sumX) / (sumX   sumX2/(sumX/2)) + sumY/2;

    /*** REPEAT FOR EACH VIEW ANGLE'S DATA SET ***/
    do {
        sumX = sumX2 = sumY = sumXY = 0;
        for (i=0; i<2; i++) {
            fscanf(radInput, "%f%f%f%f", &height, &view, &temp, &LhTheta[i]);
            sumX = sumX + Lh0[i];
            sumX2 = sumX2 + Lh0[i] * Lh0[i];
            sumY = sumY + LhTheta[i];
            sumXY = sumXY + Lh0[i] * LhTheta[i];
            }
        /*** CALCULATE SLOPE AND INTERCEPT FOR MULTI-VIEW CORRECTION ***/
        beta1 = (sumY/2 * sumX - sumXY) / (sumX/2 * sumX - sumX2);
        beta0 = (sumXY - sumY/2*sumX) / (sumX - sumX2/(sumX/2)) + sumY/2;
        fprintf(out,"    %g      %g\n", height, view);

        /*** CONVERT se_beta1 AND se_beta0 FROM RELATIVE TO ABSOLUTE VALUES ***/
        se_beta1 = beta1_tol * beta1;
        se_beta0 = beta0_tol * beta0;

        /***    CALCULATE RMS ERRORS FOR 8 TEMPERATURES ASSOCIATED
                WITH THE 8 SENSOR VOLTAGES. ***/
        for (m=0; m<8; m++) {

            /*** CONVERT VOLTAGE TO T(H,VIEW) ***/
            Tsensor[m] = (voltage[m]   voltageBB) * gain + TBB;

            /***    COMPUTE RMS VOLTAGE COMPONENT ***/
            /*** CHECK IF BEYOND TABLE; IF SO, USE PREVIOUS GAMMA ***/
            if (m < 7)
                gamma = (voltage[m+1]   voltage[m])/ (density[m+1]   density[m]);
            se_voltage = gamma * se_density[m];
```

```
/*** COMPUTE RMS TEMPERATURE-AT-SENSOR COMPONENT ***/
/***     SET RMS COMPONENT FOR BLACKBODY VOLTAGE = RMS FOR VOLTAGE ***/
se_voltageBB = se_voltage;
D_term = pow((gain * se_voltage), 2.0);
Vbb_term = pow((gain * se_voltageBB), 2.0);
G_term = pow(((voltage[m] - voltageBB) * se_gain), 2.0);
Tbb_term = pow(se_TBB, 2.0);
se_Tsensor = sqrt( D_term + Vbb_term + G_term + Tbb_term );

/*** COMPUTE RMS RADIANCE-AT-SENSOR COMPONENT ***/
/*** USE LOOK-UP-TABLE ***/
for (i=0; i<40; i++) {
    if ((TLtable[i][1] <= Tsensor[m]) && (Tsensor[m] < TLtable[i+1][1])) {
        Lsensor[m] = TLtable[i][0] + (Tsensor[m]    TLtable[i][1])
             * (TLtable[i+1][0]    TLtable[i][0]);
        se_Lsensor = (TLtable[i+1][0] - TLtable[i][0]) * se_Tsensor;
        break;
        }
    }

/*** COMPUTE RMS RADIANCE-AT-OBJECT COMPONENT ***/
/*** FIRST, COMPUTE RMS COMPONENT FOR TRANSMITTANCE ESTIMATOR ***/
secView = 1.0 / cos( view / 57.29578 );
p = 1.0 / ( pow(secView, kappa)    1.0);
se_transH0est = sqrt( pow( (p * pow(beta1, (p-1.0)) * se_beta1 ), 2.0) +
    pow( (kappa * p * p * pow(beta1, p) * log(beta1) *
    pow(secView, kappa) * tan(view/57.29578) * se_theta), 2.0));

/*** NEXT, COMPUTE RMS COMPONENT FOR Lu ESTIMATOR ***/
mess = pow(beta1, kappa2) * pow(secView, kappa1);
se_LuH0est = sqrt( pow((se_beta0/(mess    beta1)), 2.0)
    + pow(((beta0*(mess-1.0)*se_beta1/pow((mess-beta1),2.0)),2.0)
    + pow(((beta0*kappa1*mess*tan(view/57.29578)*se_theta)/
        pow((mess-beta1),2.0)),2.0)  );

/*** THEN, COMPUTE ESTIMATORS ***/
transH0est = pow(beta1, 1.0/(pow(secView, kappa)    1.0));
LuH0est = beta0 / (pow(beta1,kappa2)*pow(secView, kappa1)    beta1);

/*** FINALLY, COMBINE THE SUB-COMPONENTS ***/
Lsensor_term = pow((se_Lsensor/transH0est), 2.0);
Lu_term = pow((se_LuH0est/transH0est), 2.0);
trans_term = pow(((LuH0est-Lsensor[m])/(transH0est*transH0est)*se_transH0e
se_L0 = sqrt( Lsensor_term + Lu_term + trans_term );

/*** COMPUTE RMS BLACKBODY-EQUIVALENT COMPONENT ***/
L0 = (Lsensor[m] - LuH0est) / transH0est;
LT= (L0 - (1.0    emiss) * Ld) / emiss;
L0_term = pow((se_L0 / emiss), 2.0);
Ld_term = pow((1.0    se_Ld/emiss), 2.0);
emiss_term = pow(((Ld    L0)/(emiss*emiss)*se_emiss), 2.0);
se_LT = sqrt(L0_term + Ld_term + emiss_term);

/*** COMPUTE RMS APPARENT OBJECT TEMPERATURE COMPONENT ***/
for (i=0; i<40; i++) {
    if ((TLtable[i][0] <= LT) && (LT < TLtable[i+1][0])) {
        Tout = TLtable[i][1] + (LT    TLtable[i][0])
             / (TLtable[i+1][0] - TLtable[i][0]);
        se_Tout = se_LT / (TLtable[i+1][0]    TLtable[i][0]);
        break;
        }
```

43

```
            }
        /*** COMPUTE RMS ERROR CONTRIBUTIONS ***/
        L0_cont = L0_term / (se_LT * se_LT);
        Lsensor_cont = Lsensor_term / (se_L0 * se_L0) * L0_cont;
        D_cont = D_term / (se_Tsensor * se_Tsensor) * Lsensor_cont;
        G_cont = G_term / (se_Tsensor * se_Tsensor) * Lsensor_cont;
        Tbb_cont = Tbb_term / (se_Tsensor * se_Tsensor) * Lsensor_cont;
        trans_cont = trans_term / (se_L0 * se_L0) * L0_cont;
        Lu_cont = Lu_term / (se_L0 * se_L0) * L0_cont;
        emiss_cont = emiss_term / (se_LT * se_LT);
        Ld_cont = Ld_term / (se_LT * se_LT);
        fprintf(out,"%4.0f %6.1f %6.1f %6.1f %6.1f %6.1f %6.1f %6.1f %6.1f\n",
                Tout,se_Tout,trans_cont*100,Lu_cont*100,emiss_cont*100,
                Ld_cont*100,D_cont*100,G_cont*100,Tbb_cont*100);
        }     // END OF TEMPERATURE LOOP
    } while ( view < 60 );
  } while ( height < 8000 );

fclose( in );
fclose( radTempLUT );
fclose( radInput );
fclose( out );
}
```

Appendix C

Derivation of Unbiased Estimators of the Parameters

of a Functional Relationship

Given the set of independent and dependent observations $\{x_i, y_i\}$, $i=1,2,\ldots,N$, having measurement errors $\{\alpha_{1i}, \alpha_{2i}\}$, then both Equations 8 and 12 can be written

$$y_i = \beta_1 (x_i + \alpha_{1i}) + \beta_0 + \alpha_{2i} \qquad (C1)$$

where y_i is $L_i(H_j, \theta)$ in Equation 8 or $L_i(H, \theta_k)$ in Equation 12, β_1 is $\tau(H_j, \theta)$ in Equation 8 or β_1 in Equation 12, β_0 is $L_U(H_j, \theta)$ in Equation 8 or β_0 in Equation 12, and $x_i + \alpha_{1i}$ is $L_i(0, \theta)$ in Equation 8 or $L_i(H, \theta_j)$ in Equation 12. Assuming that the measurement errors are independent, and distributed as bivariate Gaussian random variables with zero means and equal variances σ_α^2, then the likelihood function F can be written

$$F = \left[2\pi\sigma_\alpha^2\right]^{-N} \exp\left\{\frac{-1}{2\sigma_\alpha} \sum_{i=1}^{N} \left[\alpha_{1i}^2 + \alpha_{2i}^2\right]\right\}$$

$$= \left[2\pi\sigma_\alpha^2\right]^{-N} \exp\left\{\frac{-1}{2\sigma_\alpha}\left(\sum_{i=1}^{N}\left[x_i - X_i\right]^2 + \sum_{i=1}^{N}\left[y_i - \beta_0 - \beta_1 X_i\right]^2\right)\right\} \qquad (C2)$$

where $\alpha_{1i} = x_i - X_i$, X_i is the ith true value of the independent variable, and $\alpha_{2i} = y_i - \beta_0 - \beta_1 X_i$. The maximum-likelihood estimators $\tilde{\beta}_0$ and $\tilde{\beta}_1$ of the parameters β_0 and β_1 are found by taking partial derivatives of the logarithm of the likelihood function and setting them equal to zero. Essentially following the derivation of Graybill (1961)

$$\frac{\partial \ln F}{\partial \beta_0} = \sigma_\alpha^{-2} \sum_{i=1}^{N} \left[y_i - \beta_0 - \beta_1 X_1\right] = 0, \qquad (C3)$$

$$\frac{\partial \ln F}{\partial \beta_1} = \sigma_\alpha^{-2} \sum_{i=1}^{N} \left[y_i - \beta_0 - \beta_1 X_1\right]X_1 = 0, \qquad (C4)$$

and

$$\frac{\partial \ln F}{\partial X_i} = \sigma_\alpha^{-2}\left\{[y_i - \beta_0 - \beta_1 X_i]\beta_1 + [x_i - X_i]\right\} = 0 \ \forall \ i=1,2,\dots,N. \qquad \text{(C5)}$$

Multiplying Equation C3 by $\dfrac{-\sigma_\alpha^2}{N}$, gives

$$\beta_0 + \frac{\beta_1}{N}\sum_{i=1}^{N} X_i - \overline{y} = 0 \qquad \text{(C6)}$$

where $\overline{y} = \displaystyle\sum_{i=1}^{N} \frac{y_i}{N}$. Multiplying Equation C5 by $\dfrac{\sigma_\alpha^2}{N}$, summing over all i, and rearranging, gives

$$\left[\beta_0 + \frac{\beta_1}{N}\sum_{i=1}^{N} X_i - \overline{y}\right]\beta_1 = \frac{1}{N}\sum_{i=1}^{N} [x_i - X_i]. \qquad \text{(C7)}$$

Substituting Equation C6 into C7 gives

$$\sum_{i=1}^{N} [x_i - X_i] = 0. \qquad \text{(C8)}$$

Substituting Equation C8 back into C7 gives the intercept estimator

$$\widetilde{\beta}_0 = \overline{y} - \widetilde{\beta}_1 \overline{x}. \qquad \text{(C9)}$$

Solving Equation C5 for X_i gives

$$X_i = \frac{x_1 + \beta_1 y_i - \beta_0 \beta_1}{1 + \beta_1^2}. \qquad \text{(C10)}$$

Solving Equation C4 for β_1 gives

$$\beta_1 = \frac{\displaystyle\sum_{i=1}^{N} [y_i - \beta_0]X_i}{\displaystyle\sum_{i=1}^{N} X_i^2}. \qquad \text{(C11)}$$

Substituting Equation C9 into C10, and substituting both equations into C11, multiplying C11 by -1, and simplifying gives

$$\beta_1^2\left[\sum_{i=1}^{N} (y_i-\overline{y})(x_i-\overline{x})\right] + \beta_1\left[\sum_{i=1}^{N} (x_i-\overline{x})^2 - \sum_{i=1}^{N} (y_i-\overline{y})^2\right] - \sum_{i=1}^{N} (y_i-\overline{y})(x_i-\overline{x}) = 0. \quad \text{(C12)}$$

Using the quadratic formula, the solution to Equation C12 is the slope

estimator

$$\widetilde{\beta}_1 = \pm \sqrt{U^2 + 1} + U,$$ (C13)

where

$$U = \frac{\displaystyle\sum_{i=1}^{N} [y_i - \overline{y}]^2 - \sum_{i=1}^{N} [x_i - \overline{x}]^2}{2\displaystyle\sum_{i=1}^{N} [x_i - \overline{x}][y_i - \overline{y}]}$$

$$= \frac{\displaystyle\sum_{i=1}^{N} y_i^2 - \sum_{i=1}^{N} x_i^2 + \frac{1}{N}\left[\sum_{i=1}^{N} x_i\right]^2 - \frac{1}{N}\left[\sum_{i=1}^{N} y_i\right]^2}{2\left[\displaystyle\sum_{i=1}^{N} x_i\, y_i - \frac{1}{N}\sum_{i=1}^{N} x_i \sum_{i=1}^{N} y_i\right]}$$ (C14)

and the sign of the first term is chosen which maximizes the likelihood function.

APPENDIX D

Biweight Regression Analysis

Given a first-order linear regression model

$$y_i = \beta_1 x_i + \beta_0 + e_i, \tag{D1}$$

where y_i is the ith dependent variable observation, x_i is the ith independent variable value, e_i is the ith error component, and β_1 and β_0 are the unknown parameters. The biweight regression estimators (Mosteller and Tukey 1977) of β_1 and β_0 at the mth iteration are given by

$$\ddot{\beta}_1^{(m)} = \frac{\sum_{i=1}^{N} w_i^{(m)} y_i \sum_{i=1}^{N} w_i^{(m)} x_i - \sum_{i=1}^{N} w_i^{(m)} \sum_{i=1}^{N} w_i^{(m)} x_i y_i}{\left[\sum_{i=1}^{N} w_i^{(m)} x_i\right]^2 - \sum_{i=1}^{N} w_i^{(m)} \sum_{i=1}^{N} w_i^{(m)} x_i^2} \tag{D2}$$

and

$$\ddot{\beta}_0^{(m)} = \frac{\sum_{i=1}^{N} w_i^{(m)} y_i}{\sum_{i=1}^{N} w_i^{(m)}} - \ddot{\beta}_1^{(m)} \left[\frac{\sum_{i=1}^{N} w_i^{(m)} x_i}{\sum_{i=1}^{N} w_i^{(m)}}\right], \tag{D3}$$

where

$$w_i^{(m)} = \begin{cases} (1 - u_i^2)^2, & |u_i| \le 1 \\ 0, & |u_i| > 1 \end{cases}, \tag{D5}$$

$$u_i = \frac{r_i^{(m)}}{6 s_m}, \tag{D6}$$

$$r_i^{(m)} = y_i - \ddot{\beta}_0^{(m)} - \ddot{\beta}_1^{(m)} x_i, \tag{D7}$$

and

$$s_m = \text{median}\left\{\left|r_i^{(m)}\right|\right\}. \tag{D8}$$

The initial estimates of $\hat{\beta}_0$ and $\hat{\beta}_1$ are found by a three-point median fit, i.e., divide the data in the x-direction into three groups of approximately equal sample sizes; calculate the x-median and y-median for each group; and compute a least-squares regression on these three points.

Appendix E

Error Analysis for a Film-based Sensor
using Multiple-view-angle Data

The starting point for an error analysis of a film-based thermal infrared imaging scanner is often the optical density D of objects on the film. Consider a six-step procedure: 1) density to voltage, using a step wedge on the film; 2) voltage to temperature at the sensor, using a one-point blackbody sensor calibration; 3) temperature at the sensor to radiance at the sensor, using linear interpolation in a look-up table of the integral of Planck's Law and the detector's sensitivity; 4) radiance at the sensor to radiance at the object, using the multiple-view-angle atmospheric correction technique; 5) radiance at the object to blackbody-equivalent radiance, using Equation 22; and 6) blackbody-equivalent radiance to apparent object temperature, using the inverse linear interpolation of step 3.

Step 1: Density to voltage

The voltage V of the scanner is usually calibrated to a step wedge written on the film, and assumes a piecewise-linear calibration

$$V = \gamma_i(D)\, D + V_{i0}(D), \qquad (E1)$$

where $\gamma_i(D)$ is the slope for the ith segment of the step wedge at D, and $V_{i0}(D)$ is the intercept for that i^{th} segment. Using Equation 40, the estimated standard error of the voltage is

$$\hat{\sigma}_V = \sqrt{\left[\frac{\partial V}{\partial \gamma_i(D)}\hat{\sigma}_{\gamma_i(D)}\right]^2 + \left[\frac{\partial V}{\partial D}\hat{\sigma}_D\right]^2 + \left[\frac{\partial V}{\partial V_{i0}(D)}\hat{\sigma}_{V_{i0}(D)}\right]^2}$$

$$\cong \frac{\partial V}{\partial \gamma_i(D)} \widehat{\sigma}_{\gamma_i(D)} \cong |\gamma_i(D)| \widehat{\sigma}_{\gamma_i(D)}. \tag{E2}$$

Step 2: Voltage to temperature at the sensor

Given a one-point blackbody calibration for the imaging scanner, the relationship between voltage and the temperature T at the sensor is

$$T(H,\theta) = (V - V_{bb}) G + T_{bb}, \tag{E3}$$

where V_{bb} is the sensor's voltage reading given the blackbody as input, G is the gain of the sensor, and T_{bb} is the temperature of the blackbody. Therefore

$$\widehat{\sigma}_{T(H,\theta)} = \sqrt{\left[\frac{\partial T}{\partial V}\widehat{\sigma}_V\right]^2 + \left[\frac{\partial T}{\partial V_{bb}}\widehat{\sigma}_{V_{bb}}\right]^2 + \left[\frac{\partial T}{\partial G}\widehat{\sigma}_G\right]^2 + \left[\frac{\partial T}{\partial T_{bb}}\widehat{\sigma}_{T_{bb}}\right]^2}$$

$$= \sqrt{\left[G\,\widehat{\sigma}_V\right]^2 + \left[-G\,\widehat{\sigma}_{V_{bb}}\right]^2 + \left[(V - V_{bb})\widehat{\sigma}_G\right]^2 + \widehat{\sigma}^2_{T_{bb}}}. \tag{E4}$$

Step 3: Temperature at the sensor to radiance at the sensor

Given Equation 26,

$$\widehat{\sigma}_{L(H,\theta)} \cong \left|\frac{\partial L(H,\theta)}{\partial T(H,\theta)}\right| \widehat{\sigma}_{T(H,\theta)}. \tag{E5}$$

Step 4: Radiance at the sensor to radiance at the object

Given Equation 21,

$$\widehat{\sigma}_{L(0,0)} = \sqrt{\left[\frac{\partial L(0,0)}{\partial L(H,0)}\widehat{\sigma}_{L(H,0)}\right]^2 + \left[\frac{\partial L(0,0)}{\partial \widehat{L}_U(H,0)}\widehat{\sigma}_{\widehat{L}_U(H,0)}\right]^2 + \left[\frac{\partial L(0,0)}{\partial \widehat{\tau}(H,0)}\widehat{\sigma}_{\widehat{\tau}(H,0)}\right]^2}$$

$$= \sqrt{\left[\frac{\widehat{\sigma}_{L(H,0)}}{\widehat{\tau}(H,0)}\right]^2 + \left[\frac{\widehat{\sigma}_{L_U(H,0)}}{-\widehat{\tau}(H,0)}\right]^2 + \left[\frac{\widehat{L}_U(H,0) - L(H,0)}{\widehat{\tau}^2(H,0)}\widehat{\sigma}_{\widehat{\tau}(H,0)}\right]^2}. \tag{E6}$$

Using Equation 43 as the estimator of atmospheric transmittance leads to

$$\widehat{\sigma}_{\widehat{\tau}(H,0)} = \sqrt{\left[\frac{\partial \widehat{\tau}(H,0)}{\partial \widehat{\beta}_1} \widehat{\sigma}_{\widehat{\beta}_1}\right]^2 + \left[\frac{\partial \widehat{\tau}(H,0)}{\partial \theta} \widehat{\sigma}_\theta\right]^2}$$

$$= \sqrt{\left[-p \, \widehat{\beta}_1^{\widehat{p}-1} \, \widehat{\sigma}_{\widehat{\beta}_1}\right]^2 + \left[-\kappa \, p^2 \, \widehat{\beta}_1^{\widehat{p}} \ln \widehat{\beta}_1 \, (\sec \theta)^\kappa \tan \theta \, \widehat{\sigma}_\theta\right]^2} \quad , \qquad \text{(E7)}$$

where

$$p = \frac{1}{(\sec \theta)^\kappa - 1}. \qquad \text{(E8)}$$

And, using Equation 44 as the estimator of upwelled radiance leads to

$$\widehat{\sigma}_{\widehat{L}_U(H,0)} = \sqrt{\left[\frac{\partial \widehat{L}_U(H,0)}{\partial \widehat{\beta}_0} \widehat{\sigma}_{\widehat{\beta}_0}\right]^2 + \left[\frac{\partial \widehat{L}_U(H,0)}{\partial \widehat{\beta}_1} \widehat{\sigma}_{\widehat{\beta}_1}\right]^2 + \left[\frac{\partial \widehat{L}_U(H,0)}{\partial \theta} \widehat{\sigma}_\theta\right]^2}$$

$$= \sqrt{\left[\frac{\widehat{\sigma}_{\widehat{\beta}_0}}{\widehat{\beta}_1^{\widehat{\kappa}_2}(\sec \theta)^{\kappa_1} - \widehat{\beta}_1}\right]^2 + \left[\frac{-\widehat{\beta}_0 \left\{\widehat{\beta}_1^{\widehat{\kappa}_2}(\sec \theta)^{\kappa_1} - 1\right\} \widehat{\sigma}_{\widehat{\beta}_1}}{\left\{\widehat{\beta}_1^{\widehat{\kappa}_2}(\sec \theta)^{\kappa_1} - \widehat{\beta}_1\right\}^2}\right]^2 + \left[\frac{-\widehat{\beta}_0 \, \kappa_1 \widehat{\beta}_1^{\widehat{\kappa}_2}(\sec \theta)^{\kappa_1} \tan \theta \, \widehat{\sigma}_\theta}{\left\{\widehat{\beta}_1^{\widehat{\kappa}_2}(\sec \theta)^{\kappa_1} - \widehat{\beta}_1\right\}^2}\right]^2} .$$

$$\text{(E9)}$$

Step 5: Radiance at the object to blackbody-equivalent radiance

Using Equation 22,

$$\widehat{\sigma}_{L_T} = \sqrt{\left[\frac{\partial L_T}{\partial L(0,0)} \widehat{\sigma}_{L(0,0)}\right]^2 + \left[\frac{\partial L_T}{\partial L_D} \widehat{\sigma}_{L_D}\right]^2 + \left[\frac{\partial L_T}{\partial \varepsilon} \widehat{\sigma}_\varepsilon\right]^2}$$

$$= \sqrt{\left[\frac{\widehat{\sigma}_{L(0,0)}}{-\varepsilon}\right]^2 + \left[1 - \frac{\widehat{\sigma}_{L_D}}{\varepsilon}\right]^2 + \left[\frac{L_D - L(0,0)}{\varepsilon^2} \widehat{\sigma}_\varepsilon\right]^2} . \qquad \text{(E10)}$$

Step 6: Blackbody-equivalent radiance to object temperature

And finally, analogous to Equation E5,

$$\widehat{\sigma}_T = \left|\frac{\partial T}{\partial L_T}\right| \widehat{\sigma}_{L_T}. \qquad \text{(E11)}$$

References

Beers, Y. (1957). *Introduction to the Theory of Error.* Addison-Wesley Publishing Co., Inc. pp 26–36.

Byrnes, A. E. (1983). A Comparison Study of Atmospheric Radiometric Calibration Methods for Aerial Thermograms. (unpublished) M.S. Thesis. *Rochester Institute of Technology.*

Byrnes, A. E. and J. R. Schott (1986). Correction of thermal imagery for atmospheric effects using aircraft measurement and atmospheric modeling techniques. *Applied Optics* **25**(15):2563–2570.

Chapman, R. M., J. N. Howard and E. A. Miller (1949). Atmospheric Transmission of Infrared, Summary Report. *Ohio State University Research Foundation* W44-099eng400.

Chedin, A., N. A. Scott and A. Berroir (1982). A Single-Channel, Double-Viewing Angle Method for Sea Surface Temperature Determination from Coincident METEOSAT and TIROS-N Radiometric Measurements. *Journal of Applied Metrology* **21**:613–618.

Cogan, J. L. (1985). Remote Sensing of Surface and Near Surface Temperature from Remotely Piloted Aircraft. *Applied Optics* **24**(7):1030–1036.

Cogan, J. L. (1988). Passive Remote Sensing of Slant Path Transmittance from Aircraft. *Applied Optics* **27**(15):3280–3289.

Dalu, G. (1986). Satellite Remote Sensing of Atmospheric Water Vapor *International Journal of Remote Sensing* **7**(9):1089–1097.

Diner, D. J. and J.V. Martonchik (1985). Atmospheric Transmittance from Spacecraft using Multiple View Angle Imagery *Applied Optics* **24**(21):3503–3511.

Djavadi, D. and J. M. Anderson (1987). Atmospheric Correction of Thermal Infrared Data using Multi-height Data Acquisition. *International Journal of Remote Sensing* **8**(12):1879–1884.

Graybill, F. A. (1961). An Introduction to Linear Statistical Models, Volume 1. *McGraw-Hill Book Co., Inc.* pp 186–193.

Haynes, R. B. and J. Whipple (1971). Problems in Applying Infrared Reconnaissance Technology to Water Temperature Surveillance. *Rome Air Development Center* **RADC/IR/TM-71-2**.

Holyer, R. J. (1984). A Two-satellite Method for Measurement of Sea Surface Temperature. *International Journal of Remote Sensing* **5**(1):115–131.

Kneizys, F. X., G. P. Anderson, E. P. Shettle, W. O. Gollery, L. W. Abreu, J. E. Selby, J. H. Chetwynd and S. A. Clough (1988). Users Guide to LOWTRAN 7. *Air Force Geophysics Laboratory* **AFGL-TR-88-0177**.

Kneizys, F. X., E. P. Shettle, W. O. Gollery, J. H. Chetwynd, Jr., L. W. Abreu, J. E. Selby, R. W. Fenn and R. A. McClatchey (21 February 1980). Atmospheric Transmittance/Radiance: Computer Code LOWTRAN 5. *Air Force Geophysics Laboratory* **AFGL-TR-80-0067**.

Lorenz, D. (1968). Temperature Measurements of Natural Surfaces Using Infrared Radiometers. *Applied Optics* **7**(9).

Macleod, I.D. (1984). An Airborne Thermal Remote Sensing Calibration Technique. (unpublished) M.S. Thesis. *Rochester Institute of Technology*.

Maul, G. A. (1981). Application of GOES Visible–Infrared Data to Quantifying Mesoscale Ocean Surface Temperatures. *Journal of Geophysical Research* **86**(C9):8007–8021.

McMillan, L. M. (1975). Estimation of Sea Surface Temperatures from Two Infrared Window Measurements with Different Absorption. *Journal of Geophysical Research* **80**(36).

Mosteller, F. and J. W. Tukey (1977). Data Analysis and Regression, A Second Course in Statistics. *Addison-Wesley Publishing Co.* pp. 353–365.

Prabhakara, C., G. Dalu and V. G. Kunde (1974). Estimation of Sea Surface Temperature from Remote Sensing in the 11–13 μm Window Region. *Journal of Geophysical Research* **79**(33).

Price, J. C. (1983). Estimating Surface Temperatures from Satellite Thermal Infrared Data—A Simple Formulation for the Atmospheric Effect. *Remote Sensing of Environment* **13**:353–361.

Price, J. C. (1984). Land Surface Temperature Measurements from the Split Window Channels of the NOAA 7 Advanced Very High Resolution Radiometer. *Journal of Geophysical Research* **89**(D5):7231–7237.

SAS Institute Inc. (1985). *SAS User's Guide: Statistics, Version 5 Edition*, Cray, North Carolina.

Saunders, P. M. (1967). Aerial Measurements of Sea Surface Temperature in the Infrared. *Journal of Geophysical Research* **72**:4109–4117.

Saunders, P. M. (1970). Correction for Airborne Radiation Thermometry. *Journal of Geophysical Research* **75**:7496–7601.

Scarpace, F. L. and T. Green (1973). Dynamic Surface Temperature Structure of Thermal Plumes. *Water Resources Research* **9**:138–153.

Scarpace, F. L., R. P. Madding and T. Green (1975). Scanning Thermal Plumes. *Photogrammetric Engineering and Remote Sensing* **41**(10).

Schott, J. R. and R. H. Tourin (1975). A Completely Airborne Calibration of Aerial Infrared Water Temperature Measurements. *Proceedings, ERIM 10th International Symposium on Remote Sensing of Environments, Ann Arbor, Michigan.*

Schott, J. R. (1979). Temperature Measurement of Cooling Water Discharged from Power Plants. *Photogrammetric Engineering and Remote Sensing.* **45**(6):753–761.

Schott, J. R., J. D. Biegel, and I. Macleod (1983). A Comparison of Techniques for Radiometric Calibration of Aerial Infrared Thermal Images. *Proceedings, Joint SPSE, ASP Conference on Techniques for Extraction of Information from Remotely Sensed Images.* Rochester, New York, pp 53–58.

Schott, J.R. (1989). Remote Sensing Lecture Notes—Thermal Infrared Radiometric Calibration Techniques. (unpublished) Center for Imaging Science, *Rochester Institute of Technology.*

Singh, S. M. (1984). Removal of Atmospheric Effects on a Pixel by Pixel Basis from the Thermal Infrared Data from Instruments on Satellites. The Advanced Very High Resolution Radiometer (AVHRR). *International Journal of Remote Sensing* **5**(1):161–183.

Steven, M. D. and E. M. Rollin (1986). Estimation of Atmospheric Corrections from Multiple Aircraft Imagery. *International Journal of Remote Sensing* **7**(4):481–497.

Tien, C. L. (1974). Atmospheric Corrections for Airborne Measurements of Water Surface Temperatures. *Applied Optics* **13**:1745–1746.

Wan, Z. and J. Dozier (1989). Land-Surface Temperature Measurement from Space: Physical Principles and Inverse Modeling. *IEEE Transactions on Geoscience and Remote Sensing* **27**(3):268–278.

Wilson, S. B. and J. M. Anderson (1986). The Applicability of LOWTRAN 5 Computer Code to Aerial Thermographic Data Correction. *International Journal of Remote Sensing* **7**(3):379–388.